Received 11 April 2020; accepted 5 May 2020. Date of publication 14 May 2020; date of current version 12 June 2020.

Digital Object Identifier 10.1109/OJCOMS.2020.2993611

Cognitive GFDM Full-Duplex Radios With RF Impairments and ACI Constraints

AMIRHOSSEIN MOHAMMADIAN (Student Member, IEEE), AND CHINTHA TELLAMBURA (Fellow, IEEE)

Department of Electrical and Computer Engineering, University of Alberta, Edmonton, AB T6G 1H9, Canada

CORRESPONDING AUTHOR: A. MOHAMMADIAN (e-mail: am11@ualberta.ca)

ABSTRACT We investigate the problem of sum-rate maximization of a secondary link of full-duplex generalized frequency division multiplexing (GFDM) radios operating over a spectrum hole, which is surrounded by two active primary adjacent channels. Thus, the secondary transmissions must be below an adjacent channel interference (ACI) threshold. In-band distortions and several interference terms are also caused by phase noise, in-phase (I) and quadrature (Q) imbalance, carrier frequency offset (CFO) and the nonlinear power amplifier (PA). Analog domain and digital domain self-interference (SI) cancellation is also considered. We study the two cases of two independent oscillators for local transmitter and receiver and one common shared oscillator. We derive the powers of residual SI, desired signal, interference signal and noise, signal-to-interference-plus noise ratio (SINR) and the power spectral density (PSD) of the transmit signal. By using successive convex approximations, we solve the sum-rate maximization problem. Finally, we show that in full-duplex radios under certain RF impairments, GFDM may double the sum rate compared to that of orthogonal frequency division multiplexing (OFDM).

INDEX TERMS Full-duplex radios, generalized frequency division multiplexing (GFDM), cognitive radio, spectrum hole, radio frequency (RF) impairments, rate optimization.

I. INTRODUCTION

THE CRITICAL targets of fifth generation (5G) wireless networks include 1000 times increase in the data rate, below 100 ms latency, 50% network cost reduction, and 95% availability in bad coverage locations [1], [2]. However, 5G faces the challenge of spectrum crunch because much of the sub-6 GHz spectrum is more or less fully assigned to existing services and applications. Moreover, new wireless applications and services are massive bandwidth users. Thus, to overcome the spectrum crunch, spectral efficiency gains are essential. It is widely agreed that 5G wireless networks require 10 times spectral efficiency of current 4G systems [3]. Thus, several key technologies are being considered.

1) Spectral efficiency can be potentially doubled with the use of full-duplex radios with simultaneous transmission and reception on the same frequency band. Thus, they can potentially double the network capacity, reduce network delay, and improve network secrecy [4], [5]. However, these potential gains may not be fully realized because full-duplex radios are limited by self-interference (SI), which can be as high as 100 dB above the noise floor of the local receiver [6], [7].
2) Spectral efficiency may also be improved by replacing orthogonal frequency division multiplexing (OFDM), which is the basis for the fourth generation long term evolution (4G-LTE) standard. However, OFDM maybe susceptible to several issues including excessive signal peaks [8], [9]. Thus, generalized frequency division multiplexing (GFDM) has emerged as a potential competitor of OFDM. GFDM is a flexible non-orthogonal multi-carrier waveform which includes number of subcarriers, each one carries subsymbols generated in multiple time slots. GFDM has the advantages of low out-of-band emissions, high spectral efficiency and low latency [10], [11] and multiple applications [12]–[16]. Thus, GFDM-based full-duplex radio transceivers may help to achieve the aforementioned 5G performance targets.
3) Another path for spectral efficiency gains is the use of cognitive radio networks to more efficiently utilize the

spectrum. Moreover, cognitive full-duplex radios can enhance spectrum sensing, reduce latency, minimize data loss and improve spectrum utilization [17]. While there are several cognitive radio modes, the simplest option is to allow secondary users (SUs) to access a spectrum hole [18]. A spectrum hole is an unused frequency band at a specific time or location in which primary users (PUs) are not transmitting [19].

In this work, we integrate the above three technologies; namely full-duplex GFDM transceivers operating over a spectrum hole. The spectrum hole is however considered to be in a highly congested spectral region. Thus, it lies between two active primary channels. This means that if SUs communicate in it, they have to respect adjacent channel interference constraints. We feel that this scenario offers a realistic model in the face of high capacity networks. Moreover, as mentioned before, although full-duplex may double the spectral efficiency in principle, SI can diminish much of the gains. For this reason, SI cancellation algorithms for full-duplex radios have been intensively researched [20]. Nevertheless, the performance of such algorithms degrades due to the radio frequency (RF) impairments – namely phase noise, in-phase (I) and quadrature phase (Q) imbalance, carrier frequency offset (CFO), and power amplifier (PA) non-linearity.

Therefore, our main goal is to quantify and analyze the effects of these impairments on the considered system. A further motivating factor is that these are the most significant impairments due to common hardware imperfections and hence their effects have been widely investigated. For instance, the impact of phase noise [21], [22], IQ imbalance [23], [24], CFO [25], and nonlinear PA [26], [27] on full-duplex OFDM transceivers have been studied. Thus, phase noise can cause 15 dB residual SI above the noise floor [28] and can increase SI power in full-duplex radios [21], [24]. Moreover, the IQ imbalance generates an interference image signal roughly 25 dB below the desired signal [27], which degrades the spectrum sensing capability of cognitive full-duplex networks [29]. The CFO results in inter-carrier interference [25]. The collective impact of a nonlinear PA and an IQ imbalance is investigated in [26]. For a half-duplex OFDM cognitive network in the presence of RF impairments, optimal power allocation has been studied in [30]. The impact of RF impairments on half-duplex GFDM systems has also been studied [31]–[33]. All in all, these previous studies clearly show that the RF imperfections significantly degrade the performance of the SI cancellation techniques by introducing in-band and out-of-band distortions and interference terms. In this paper, we add a new wrinkle by considering the ACI constraints, which are critical in cognitive networks [34].

A. PROBLEM TACKLED IN THIS WORK

We now describe it in detail. The spectrum hole $[f_2, f_3]$ and the upper band $[f_3, f_4]$ and lower band $[f_1, f_2]$ adjacent to it are shown in Fig. 1. These two bands contain two active PUs. The spectrum hole (Fig. 2) is accessed by two nodes,

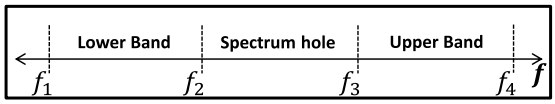

FIGURE 1. Spectrum hole and two adjacent bands.

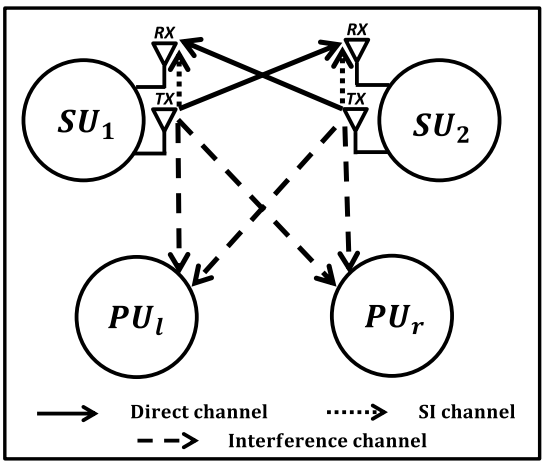

FIGURE 2. The full-duplex cognitive radio link.

say, SU_1 and SU_2 (full-duplex transceivers). The full-duplex link between these two nodes is the secondary link under consideration. According to cognitive radio principles, the operation of secondary links must be controlled to minimize any potential harm on primary users. Therefore, in our system model, the ACI levels must be below an interference threshold.

In this network, the performance of the secondary link depends on the RF impairments, which in turn result in in-band distortion, self-interference, noise and ACI. Although ACI can be controlled with the use of GFDM, which uses non-orthogonal sub-carriers to reduce out-of-band emissions, the drawback is the in-band distortion. If SU_1 and SU_2 increase their transmit powers, then the ACI constraints could be violated. In sum, the secondary link rate depends on many tightly coupled, conflicting factors. Is it better to use GFDM than OFDM? To answer these questions, we should model the system in detail. Practical RF impairments and active SI cancellation in both analog and digital domain for full-duplex transceivers should be considered. Furthermore, this exact system model but for the half-duplex GFDM was studied in [19], [35]. These works developed an optimal power allocation for maximizing the secondary sum rate.

Furthermore, to the best of our knowledge, the GFDM full-duplex link over a spectrum hole has not been investigated by considering active analog and digital SI cancellations, phase noise, IQ imbalance, CFO and nonlinear PA.

B. WORK CONTRIBUTIONS

In this paper, we study the GFDM-based full-duplex link over a spectrum hole with two neighboring active PUs (Fig. 2). Both active analog and digital cancellations and phase noise,

IQ imbalance, CFO, and nonlinear PA are considered. Two configurations are addressed for transmitter and receiver oscillators in a full-duplex node: 1) two separate oscillators, and 2) one common oscillator. Desired, interference and SI channels are modeled as frequency selective, a natural assumption for high data rate systems. Our main goals are to analyze the effects of RF impairments and also to maximize the sum rate of SU link under the ACI constraints on the two PU channels.

This paper makes the following contributions:

- We establish a system model in which GFDM-based full-duplex secondary link operates in a spectrum hole whose lower and upper adjacent bands are active PUs. We theoretically model GFDM full-duplex transceivers in details based on well-known GFDM modulator/demodulator, existing SI cancellation methods and practical RF impairments models. Active analog and digital cancellation techniques and RF impairments including phase noise, IQ imbalance, CFO, and nonlinear PA are addressed. Note that in [36], we considered two independent oscillators for local transmitter and receiver. In contrast, in this paper, we analyze the system with one common shared oscillator, as well. Moreover, a third-order nonlinear PA is assumed.
- Powers of residual SI, desired signal and noise are derived in closed form. Moreover, signal-to-interference-plus noise ratio (SINR) is derived. Furthermore, we derive the power spectral density (PSD) of the transmit signal and use it to quantify the adjacent channel interference (ACI) on the PU channels. None of these expressions have been derived before.
- The sum rate of the SU link is maximized under the constraints of maximum tolerable interference power on PU bands. Since this problem is non-convex, successive convex approximations is deployed to convert the problem to standard geometric programming (GP). Note that deriving the sum rate and solving the power allocation problem have not done before.
- The resulting problem is solved via common CVX tool [37]. All the theoretical derivations are verified with simulation results. To determine the performance gains of full-duplex GFDM, we present full-duplex OFDM results. Note that even for full-duplex OFDM, the interweave cognitive network (Fig. 2) has not been investigated previously.

In a related work [38], we modeled and analyzed the GFDM-modulated full-duplex link operating in a spectrum hole. We considered phase noise, IQ imbalance, and CFO. Furthermore, optimal power for maximizing sum rate of SU link under the constraints of maximum tolerable interference power on PU bands was derived. In this current paper, we greatly extend [38] and consider the impact of the nonlinear power amplifier. This impact generates several in-band and out-of-band interference terms and the structure of digital-domain SI cancellation becomes more complicated. Moreover, this work studies the in-band interference terms and spectral regrowth caused by nonlinear PA.

On the other hand, for full-duplex GFDM, digital SI cancellation is investigated in [39] and SI power is derived. In [36], [40], we model and analyze the full-duplex GFDM transceiver in presence of phase noise, IQ imbalance and CFO by considering both analog and digital cancellations and propose receiver filter to maximize the desired signal-to-interference ratio. Note that two independent oscillators for local transmitter and receiver of full-duplex node was considered.

This paper is organized as follows. Section II presents the system model. Section III analyzes the powers of various signal components and derives the SINR. Section IV derives the PSD of the transmitted signal and formulates the ACIs on lower and upper PUs. Section V develops an algorithm to compute the maximum sum rate of the SU link. Simulation and numerical results in Section VI verify the accuracy of the derived results. Moreover, the maximized sum rate is illustrated for different setups. Finally, concluding remarks are provided in Section VII.

II. SYSTEM MODEL

The full-duplex cognitive radio link in Fig. 2 uses GFDM and has two full-duplex nodes (as SU_1 and SU_2) in the presence of phase noise, IQ imbalance, CFO and nonlinear PA. As mentioned before, the effects of the transmissions of SU_1 and SU_2 must not exceed the ACI thresholds. We assume that negligible interference on SU_1 and SU_2 from PU transmissions (if any).

The channel coefficient SU_i to SU_j is h_{ij}, $i,j \in \{1,2\}$ and $i \neq j$. The channel coefficient h_{ii}, $i \in \{1,2\}$ represents the SI channel at SU_i. Furthermore, $h_{l,i}$ and $h_{r,i}$, $i \in \{1,2\}$, represent the channels between SU_i and lower and upper active PUs, respectively.

Without loss of generality, we take SU_1 to analyze the signal model and SI cancellation process in detail. Thus, SU_1 transmits the data of M time slots with K subcarriers, and the discrete GFDM signal per frame may be expressed as

$$x_1[n] = \sqrt{p_1} \sum_{k=0}^{K-1} \sum_{m=0}^{M-1} d_{k,m}^1 g_m[n] e^{\frac{j2\pi kn}{K}} \tag{1}$$

where $0 \leq n \leq MK-1$, p_1 is the average transmit power, $d_{k,m}^1$, $k = 1, 2, \ldots, K$ and $m = 1, 2, \ldots, M$ are independent and identically distributed (i.i.d.) complex data symbols with zero mean and unit variance and $g_m[n] = g[n - mK]_{MK}$ is a circularly shifted version of normalized prototype filter $g[n]$ ($\sum_{n=0}^{MK-1} |g[n]|^2 = 1$). After digital to analog converter, the analog GFDM baseband signal $x_1(t)$ goes through the IQ mixer, which has certain non-zero IQ imbalance. Thus, the IQ and phase noise impaired signal may be written as [26]

$$y_1^{IQ}(t) = \left(g_{Tx,d} x_1(t) + g_{Tx,I} x_1^*(t)\right) e^{j\phi_{Tx,1}(t)} \tag{2}$$

where $(.)^*$ indicates complex conjugate, $g_{Tx,d}$ and $g_{Tx,I}$ are the transmitter IQ mixer responses for the direct and image

signals, respectively, and $\phi_{Tx,1}(t)$ is random phase noise of the local oscillator of the SU_1 local transmitter. Image rejection ratio (IRR) is considered for quantifying the quality of the IQ mixer which is defined as $\text{IRR}_{Tx} = \frac{|g_{Tx,I}|^2}{|g_{Tx,d}|^2}$.

We consider the PA response is modeled by a third-order Hammerstein nonlinearity [27] as

$$y_1(t) = a_1 y_1^{IQ}(t) + a_3 y_1^{IQ}(t)|y_1^{IQ}(t)|^2 \tag{3}$$

where a_1 and a_3 are linear and third-order gains. Moreover, $y_1^{IQ}(t)|y_1^{IQ}(t)|^2$ can be approximated by $(g_{Tx,d}x_{PA,1}(t) + g_{Tx,I}x^*_{PA,1}(t))e^{j\phi_{Tx,1}(t)}$ [27], where $x_{PA,1}(t) = x_1(t)|x_1(t)|^2$. Note that Hammerstein model is widely used in literature for characterizing a nonlinear PA [26], [27], [30], [41]. Moreover, a third order polynomial is considered since it is the strongest nonlinearity and model the behaviour of nonlinear PA precisely [30]. However, other PA setups, e.g., generic baseband model [42], can be considered for comparison which we leave this for future works. The central limit theorem tells us that, when $MK \to \infty$, the GFDM signal sample Gaussian distributed [35]. Thus, following the Bussgang theorem [30], [35], the output of the Hammerstein nonlinear PA can be written as summation of a linear scaling of the input signal and nonlinear distortion noise.

The output signal $y_1(t)$ is transmitted to SU_2 through wireless channel $h_{12}(t)$ and a part of it leaks to the SU_1 local receiver through the SI channel $h_{11}(t)$. Thus, the received signal at the local receiver of SU_1, including the SI signal and the signal-of-interest from SU_2, is given by

$$r_1(t) = y_2(t) * h_{21}(t) + y_1(t) * h_{11}(t) + n_1(t) \tag{4}$$

where $*$ denotes the convolution, $y_2(t)$ is the desired transmitted signal from SU_2, and $n_1(t)$ is a circular symmetric complex Gaussian noise with zero mean and variance σ_n^2. By assuming IQ mixer responses of SU_2 same as SU_1, $y_2(t)$ may be written as

$$y_2(t) = a_1 y_2^{IQ}(t) + a_3 y_2^{IQ}(t)|y_2^{IQ}(t)|^2 \tag{5}$$

where $y_2^{IQ}(t)$ is equal to

$$y_2^{IQ}(t) = \left(g_{Tx,d}x_2(t) + g_{Tx,I}x_2^*(t)\right)e^{j\phi_{Tx,2}(t)} \tag{6}$$

where $\phi_{Tx,2}(t)$ is random phase noise of the local oscillator of the SU_2 local transmitter and $x_2(t)$ is the analog GFDM baseband signal similar to (1) with the average transmit power p_2 and i.i.d input symbols of $d^2_{k,m}$.

At the first stage of SU_1 local receiver, active analog cancellation is employed to suppress the strong SI signal by subtracting the analog reconstruction signal. Thus, the resulting signal may be written in general form as

$$\hat{r}_1(t) = y_2(t) * h_{21}(t) + y_1(t) * h_1(t) + n_1(t) \tag{7}$$

where $h_1(t) = h_{11}(t) - h_{ALC}(t)$ is the residual SI channel and $h_{ALC}(t)$ is estimate of the SI channel [27]. Note that analog SI cancellation typically achieves 30 dB attenuation [21]. Following the active analog cancellation, attenuated received signal $\hat{r}_1(t)$ goes through the receiver IQ mixer. By taking into account the IQ imbalance and CFO between the local oscillators of the transmitter and receiver of SU_1, the output signal may be expressed as

$$\begin{aligned} r_{IQ,1}(t) = {} & g_{Rx,d}\hat{r}_1(t)e^{-j\phi_{Rx,1}(t)}e^{j2\pi\Delta_f t} + g_{Rx,I}\hat{r}_1^*(t)e^{j\phi_{Rx,1}(t)} \\ & \times e^{-j2\pi\Delta_f t} \end{aligned} \tag{8}$$

where $g_{Rx,d}$ and $g_{Rx,I}$ are the receiver IQ mixer responses for the direct and image signals. $\phi_{Rx,1}(t)$ is random phase noise of the local oscillator of SU_1 local receiver and Δ_f indicates the difference between carrier frequency of the receiver and transmitter local oscillators. Notice that oscillator of SU_1 receiver and SU_2 transmitter are independent of each other. However, in this paper, we consider two different scenarios for oscillators of SU_1 transmitter and receiver: 1) two separate oscillators where $\phi_{Tx,1}(t)$ and $\phi_{Rx,1}(t)$ are statistically independent random processes and 2) single shared oscillator where $\phi_{Tx,1}(t) = \phi_{Rx,1}(t)$.

Following the IQ mixer, the baseband analog signal $r_{IQ,1}(t)$ is then converted to discrete samples. We model $h_{21}[n]$ and $h_1[n]$ by multipath fading channels with L_1 and L_2 paths ($h_{21}[n] = \sum_{l_1=0}^{L_1-1} h_{21,l_1}\delta[n-l_1]$ and $h_1[n] = \sum_{l_2=0}^{L_2-1} h_{1,l_2}\delta[n-l_2]$), respectively. The sampled is expressed as

$$\begin{aligned} r_{IQ}[n] = {} & \sum_{l_1=0}^{L_1-1} a_1\Big(h_{21}^I[n,l_1]x_2[n-l_1] + h_{21}^Q[n,l_1]x_2^*[n-l_1]\Big) \\ & + a_3\Big(h_{21}^I[n,l_1]x_{PA,2}[n-l_1] + h_{21}^Q[n,l_1]x_{PA,2}^*[n-l_1]\Big) \\ & + \sum_{l_2=0}^{L_2-1} a_1\Big(h_1^I[n,l_2]x_1[n-l_2] + h_1^Q[n,l_2]x_1^*[n-l_2]\Big) \\ & + a_3\Big(h_1^I[n,l_2]x_{PA,1}[n-l_2] + h_1^Q[n,l_2]x_{PA,1}^*[n-l_2]\Big) \\ & + n_1^I[n] + n_1^Q[n] \end{aligned} \tag{9}$$

where equivalent desired and residual SI channels responses and equivalent noise components for the individual signal components can be written as

$$\begin{aligned} h_{21}^I[n,l_1] = {} & g_{Tx,d}g_{Rx,d}h_{21,l_1}e^{j(\phi_{TX,2}[n-l_1]-\phi_{RX,1}[n])}e^{\frac{j2\pi\epsilon n}{K}} \\ & + g^*_{Tx,I}g_{Rx,I}h^*_{21,l_1}e^{-j(\phi_{TX,2}[n-l_1]-\phi_{RX,1}[n])}e^{\frac{-j2\pi\epsilon n}{K}} \\ h_{21}^Q[n,l_1] = {} & g_{Tx,I}g_{Rx,d}h_{21,l_1}e^{j(\phi_{TX,2}[n-l_1]-\phi_{RX,1}[n])}e^{\frac{j2\pi\epsilon n}{K}} \\ & + g^*_{Tx,d}g_{Rx,I}h^*_{21,l_1}e^{-j(\phi_{TX,2}[n-l_1]-\phi_{RX,1}[n])}e^{\frac{-j2\pi\epsilon n}{K}} \\ h_1^I[n,l_2] = {} & g_{Tx,d}g_{Rx,d}h_{1,l_2}e^{j(\phi_{TX,1}[n-l_2]-\phi_{RX,1}[n])}e^{\frac{j2\pi\epsilon n}{K}} \\ & + g^*_{Tx,I}g_{Rx,I}h^*_{1,l_2}e^{-j(\phi_{TX,1}[n-l_2]-\phi_{RX,1}[n])}e^{\frac{-j2\pi\epsilon n}{K}} \\ h_1^Q[n,l_2] = {} & g_{Tx,I}g_{Rx,d}h_{1,l_2}e^{j(\phi_{TX,1}[n-l_2]-\phi_{RX,1}[n])}e^{\frac{j2\pi\epsilon n}{K}} \\ & + g^*_{Tx,d}g_{Rx,I}h^*_{1,l_2}e^{-j(\phi_{TX,1}[n-l_2]-\phi_{RX,1}[n])}e^{\frac{-j2\pi\epsilon n}{K}} \\ n_1^I[n] = {} & g_{Rx,d}e^{-j\phi_{RX,1}[n]}e^{\frac{j2\pi\epsilon n}{K}}n_1[n] \\ n_1^Q[n] = {} & g_{Rx,I}e^{j\phi_{RX,1}[n]}e^{\frac{-j2\pi\epsilon n}{K}}n_1^*[n] \end{aligned} \tag{10}$$

where ϵ represents the CFO which is normalized by subcarrier spacing (labeled as normalized CFO). Obviously, the

digital baseband signal (9) contains not only linear components but also its complex conjugate. Then, the resulted samples are sent to GFDM demodulator which the transmitted symbol from SU_2 at k'-th subcarrier and m'-th time-slot is detected by

$$\begin{aligned}\widehat{d}^{2}_{k',m'} &= \sum_{n=0}^{MK-1} (r_{IQ}[n]) f_{m'}[n] e^{\frac{-j2\pi k' n}{K}} \\ &= R^{21}_{k',m'} + R^{1}_{k',m'} + w^{eq,I}_{k',m'} + w^{eq,Q}_{k',m'} \end{aligned} \tag{11}$$

where $f_{m'}[n] = f[n - m'K]_{MK}$ is circularly shifted version of receiver filter impulse response $f[n]$. Moreover, $R^{21}_{k',m'} = R^{21,I}_{k',m'} + R^{21,Q}_{k',m'} + R^{21,PA,I}_{k',m'} + R^{21,PA,Q}_{k',m'}$ is a corresponding term of the received signal from SU_2 transmitter after GFDM demodulation, where $R^{21,I}_{k',m'}, R^{21,Q}_{k',m'}, R^{21,PA,I}_{k',m'}, R^{21,PA,Q}_{k',m'}$ are intended signal components in (9) applied to GFDM demodulator. Furthermore, $R^{1}_{k',m'} = R^{1,I}_{k',m'} + R^{1,Q}_{k',m'} + R^{1,PA,I}_{k',m'} + R^{1,PA,Q}_{k',m'}$ is a corresponding term of the residual SI signal from SU_1 receiver after GFDM demodulation, where $R^{1,I}_{k',m'}, R^{1,Q}_{k',m'}, R^{1,PA,I}_{k',m'}, R^{1,PA,Q}_{k',m'}$ residual SI signal components in (9) applied to GFDM demodulator. Finally, $w^{eq,I}_{k',m'}$ and $w^{eq,Q}_{k',m'}$ are corresponding linear and conjugate equivalent noise terms. The samples (9) go into the GFDM demodulator.

At the output the GFDM demodulator, active digital cancellation is applied by deploying the replica of transmitted symbols and their conjugate, $d^{1}_{k',m'}$ and $d^{*1}_{k',m'}$, and estimation of the linear equivalent residual SI channel and conjugate equivalent residual SI channel, $\hat{h}^{I}_{1}[n, l_2]$ and $\hat{h}^{Q}_{1}[n, l_2]$ [36]. The output of active digital cancellation may thus be expressed as

$$\widehat{d}^{2,DLC}_{k',m'} = d^{2,s}_{k',m'} + d^{21}_{k',m'} + d^{RSI,1}_{k',m'} + w^{eq,I}_{k',m'} + w^{eq,Q}_{k',m'} \tag{12}$$

where $d^{21}_{k',m'} = R^{21}_{k',m'} - d^{2,s}_{k',m'}$ is interference of SU_2, $d^{RSI,1}_{k',m'} = R^{1}_{k',m'} - R^{DLC,I}_{k',m'} - R^{DLC,Q}_{k',m'}$ is residual SI of SU_1, and $d^{2,s}_{k',m'}$ is the desired symbol which is extracted from $R^{21}_{k',m'}$ as

$$\begin{aligned} d^{2,s}_{k',m'} = \sqrt{p_2} d^{2}_{k',m'} \sum_{l_1=0}^{L_1-1} \sum_{n=0}^{MK-1} (a_1 + 2Ka_3 p_2 \gamma[n - l_1]) \\ \times\ h^{I}_{21}[n, l_1] f_{m'}[n] g_{m'}[n - l_1] e^{\frac{-j2\pi k' l_1}{K}} \end{aligned} \tag{13}$$

where $\gamma[n] = \sum_{m=0}^{M-1} |g_m[n]|^2$.

Proof: See Appendix A. ∎

Moreover, $R^{DLC,I}_{k',m'}$ and $R^{DLC,Q}_{k',m'}$ are linear and conjugate active digital cancellation symbols, which are generated by

$$\begin{aligned} R^{DLC,I}_{k',m'} = \sqrt{p_1} d^{1}_{k',m'} \sum_{l_2=0}^{L_2-1} \sum_{n=0}^{MK-1} \hat{h}^{I}_{1}[n, l_2] \\ \times\ (a_1 + 2Ka_3 p_1 \gamma[n - l_2]) \\ \times\ f_{m'}[n] g_{m'}[n - l_2] e^{\frac{-j2\pi k' l_2}{K}} \end{aligned} \tag{14}$$

$$\begin{aligned} R^{DLC,Q}_{k',m'} = \sqrt{p_1} d^{*1}_{k',m'} \sum_{l_2=0}^{L_2-1} \sum_{n=0}^{MK-1} \hat{h}^{Q}_{1}[n, l_2] \\ \times\ (a_1 + 2Ka_3 p_1 \gamma[n - l_2]) \\ \times\ f_{m'}[n] g^{*}_{m'}[n - l_2] e^{\frac{-j2\pi k' (2n - l_2)}{K}}. \end{aligned}$$

Proof: See Appendix B. ∎

In (12), non-orthogonal subcarriers of GFDM and residual SI signal due to RF impairments cause inter carrier interference and inter symbol interference.

III. POWER ANALYSIS AND SINR DERIVATION

Here, the SINR of the desired signal transmitted from SU_2 to SU_1 given the RF impairments is analyzed. For this goal, we extract the power levels of different components in (12) including the desired signal, interference signal, residual SI signal and thermal noise. Note that two distinct oscillator configurations for local transmitter and receiver of SU_1 are studied in detail, namely 1) two separate oscillators and 2) single shared oscillator. As a starting point, we deploy standard models to characterize the phase noise and multipath channels. Thus, the free-running oscillator model with Brownian motion [31] is used to generate phase noise $[\phi[n+1] - \phi[n]] \sim \mathcal{N}(0, 4\pi\beta T_s)$, where $\phi[n]$ is Brownian motion with 3-dB bandwidth of β and the autocorrelation of $\phi[n]$ is

$$\mathbb{E}\left[e^{j\phi[n_1]} e^{-j\phi[n_2]} \right] = e^{-2|n_1 - n_2|\pi\beta T_s} \tag{15}$$

where $\mathbb{E}[.]$ indicates the statistical expectation operator. Furthermore, we assume that all the channels (h_{ij}, h_{ii}, $h_{l,i}$ and $h_{r,i}$) are wide-sense stationary uncorrelated scattering processes. Each is a mutually independent set of multipath components.

A. POWER OF THE DESIRED SYMBOL

Let $\mathbb{E}[h_{21,l_1}] = 0$ and $\mathbb{E}[|h_{21,l_1}|^2] = \sigma^2_{21,l_1}$, $l_1 = 0, \ldots, L_1$. The power of the desired symbol $d^{2,s}_{k',m'}$, derived in (13), is given by $p^{2,s}_{k',m'} = \mathbb{E}[|d^{2,s}_{k',m'}|^2] = p_2 T^{2,s,1}_{k',m'} + p_2^2 T^{2,s,2}_{k',m'} + p_2^3 T^{2,s,3}_{k',m'}$, $T^{2,s,1}_{k',m'}$, $T^{2,s,2}_{k',m'}$ and $T^{2,s,3}_{k',m'}$ are derived as

$$\begin{aligned} T^{2,s,1}_{k',m'} = |a_1|^2 \sum_{l_1=0}^{L_1-1} \sum_{n_1=0}^{MK-1} \sum_{n_2=0}^{MK-1} \sigma^2_{21,l_1} f_{m'}[n_1] f^{*}_{m'}[n_2] e^{-4|n_1 - n_2|\pi\beta T_s} \\ \times \left(|g_{TX,d} g_{RX,d}|^2 e^{\frac{j2\pi(n_1 - n_2)\epsilon}{K}} + |g_{TX,I} g_{RX,I}|^2 \right. \\ \left. \times\ e^{\frac{-j2\pi(n_1 - n_2)\epsilon}{K}} \right) g_{m'}[n_1 - l_1] g^{*}_{m'}[n_2 - l_1], \end{aligned} \tag{16}$$

$$\begin{aligned} T^{2,s,2}_{k',m'} = 4K\Re[a_1 a_3^*] \sum_{l_1=0}^{L_1-1} \sum_{n_1=0}^{MK-1} \sum_{n_2=0}^{MK-1} \sigma^2_{21,l_1} f_{m'}[n_1] f^{*}_{m'}[n_2] \\ \times\ e^{-4|n_1 - n_2|\pi\beta T_s} \left(|g_{TX,d} g_{RX,d}|^2 e^{\frac{j2\pi(n_1 - n_2)\epsilon}{K}} \right. \\ \left. + |g_{TX,I} g_{RX,I}|^2 e^{\frac{-j2\pi(n_1 - n_2)\epsilon}{K}} \right) \\ \times\ g_{m'}[n_1 - l_1] g^{*}_{m'}[n_2 - l_1] \gamma[n_1 - l_1] \end{aligned} \tag{17}$$

and

$$T^{2,s,3}_{k',m'} = 4K^2|a_3|^2 \sum_{l_1=0}^{L_1-1}\sum_{n_1=0}^{MK-1}\sum_{n_2=0}^{MK-1} \sigma^2_{21,l_1} f_{m'}[n_1] f^*_{m'}[n_2] \times e^{-4|n_1-n_2|\pi\beta T_s}\left(|g_{TX,d}g_{RX,d}|^2 e^{\frac{j2\pi(n_1-n_2)\epsilon}{K}} + |g_{TX,I}g_{RX,I}|^2 e^{\frac{-j2\pi(n_1-n_2)\epsilon}{K}}\right) \times g_{m'}[n_1-l_1] g^*_{m'}[n_2-l_1]\gamma[n_1-l_1]\gamma[n_2-l_1]. \quad (18)$$

Proof: See Appendix C. ■

Throughout the paper, $\Re[x]$ indicates the real part of x. Note that oscillators in SU_2 transmitter, $\phi_{Tx,2}(t)$, and SU_1 receiver, $\phi_{Rx,1}(t)$, are independent. Clearly, the power of the desired symbol depends on the impairments including phase noise, IQ imbalance, CFO and nonlinear PA.

B. INTERFERENCE POWERS

The power of interference terms in output of active digital cancellation (12) caused by the desired signal, $d^{21}_{k',m'} = R^{21}_{k',m'} - d^{2,s}_{k',m'}$, should be derived. It can be readily shown in Appendix A that, $d^{21}_{k',m'}$ and $d^{2,s}_{k',m'}$ are independent. Thus, total interference power can be derived by $p^{21}_{k',m'} = p^{21,t}_{k',m'} - p^{2,s}_{k',m'}$, where $p^{21,t}_{k',m'} = \mathbb{E}[|R^{21}_{k',m'}|^2]$. Due to the independence among complex data, channel coefficients and phase noise terms, after vanishing several cross terms that are equal to zero, $p^{21,t}_{k',m'} = p_2 T^{21,t,1}_{k',m'} + p_2^2 T^{21,t,2}_{k',m'} + p_2^3 T^{21,t,3}_{k',m'}$, where $T^{21,t,1}_{k',m'}$, $T^{21,t,2}_{k',m'}$ and $T^{21,t,3}_{k',m'}$ are derived as

$$T^{21,t,1}_{k',m'} = K|a_1|^2 \sum_{l_1=0}^{L_1-1}\sum_{n=0}^{MK-1}\sum_{m_1,m_2=0}^{MK-1} \sigma^2_{21,l_1} f_{m'}[n] f_{(m'+m_1)_M}[n] \times e^{-4\pi\beta T_s m_1 K}\left(|g_{TX,d}|^2 + |g_{TX,I}|^2\right) \times \left(|g_{RX,d}|^2 e^{\frac{j2\pi\epsilon(n-\zeta[n,m_1])}{K}} + |g_{RX,I}|^2 e^{-\frac{j2\pi\epsilon(n-\zeta[n,m_1])}{K}}\right) \times g_{m_2}[n-l_1] g_{(m_2+m_1)_M}[n-l_1], \quad (19)$$

$$T^{21,t,2}_{k',m'} = 4K^2\Re\left[a_1 a_3^*\right] \sum_{l_1=0}^{L_1-1}\sum_{n=0}^{MK-1}\sum_{m_1,m_2,m_3=0}^{MK-1} \sigma^2_{21,l_1} f_{m'}[n] \times f_{(m'+m_1)_M}[n] e^{-4\pi\beta T_s m_1 K}\left(|g_{TX,d}|^2 + |g_{TX,I}|^2\right) \times \left(|g_{RX,d}|^2 e^{\frac{j2\pi\epsilon(n-\zeta[n,m_1])}{K}} + |g_{RX,I}|^2 e^{-\frac{j2\pi\epsilon(n-\zeta[n,m_1])}{K}}\right) \times g_{m_2}[n-l_1] g_{(m_1+m_2)_M}[n-l_1] |g_{(m_1+m_3)_M}[n-l_1]|^2 \quad (20)$$

and

$$T^{21,t,3}_{k',m'} = K^3|a_3|^2 \sum_{l_1=0}^{L_1-1}\sum_{n=0}^{MK-1}\sum_{m_1,m_2,m_3,m_4=0}^{MK-1} \sigma^2_{21,l_1} f_{m'}[n] \times f_{(m'+m_1)_M}[n] e^{-4\pi\beta T_s m_1 K}\left(|g_{TX,d}|^2 + |g_{TX,I}|^2\right) \times \left(|g_{RX,d}|^2 e^{\frac{j2\pi\epsilon(n-\zeta[n,m_1])}{K}} + |g_{RX,I}|^2 e^{-\frac{j2\pi\epsilon(n-\zeta[n,m_1])}{K}}\right) \times g_{m_3}[n-l_1] g_{(m_3+m_1)_M}[n-l_1] g_{m_4}[n-l_1] g_{(m_1+m_2)_M} \times [n-l_1]\big(4g_{m_4}[n-l_1] g_{(m_1+m_2)_M}[n-l_1] + 2g_{m_2}[n-l_1] g_{(m_1+m_4)_M}[n-l_1]\big]). \quad (21)$$

Proof: See Appendix D. ■

Throughout the paper, $(x)_M$ denotes the operation x modulo M and $\zeta[n,m_1] = (n - m_1 K)_{MK}$. To reduce complexity, we deploy $\sum_{k=0}^{K-1} e^{-j2\pi\frac{k(n_1-n_2)}{K}} = K\sum_{t=0}^{M-1}\delta(n_1-n_2-tK)$. Obviously, the interference power terms depend on the desired channel multipath profile, 3-dB phase noise bandwidth, IQ imbalance coefficients, normalized CFO, nonlinear PA coefficients and GFDM parameters.

C. POWER OF THE RESIDUAL SI SIGNAL

We next derive the power of residual SI after active digital cancellation. In [36], the same is done for separate oscillator for transmitter and receiver of SU_1 without considering nonlinear PA. We first derive the power of active digital cancellation symbols in (14). Note that $\mathbb{E}[h_{1,l_2}] = 0$ and $\mathbb{E}[|h_{1,l_2}|^2] = \sigma^2_{1,l_2}$. The sum power of two active digital cancellation symbols in (12) can be written as $p^{11,s}_{k',m'} = \mathbb{E}[|R^{DLC,I}_{k',m'} + R^{DLC,Q}_{k',m'}|^2]$. Since $R^{DLC,I}_{k',m'}$ and $R^{DLC,Q}_{k',m'}$ are independent, we have $p^{11,s}_{k',m'} = \mathbb{E}[|R^{DLC,I}_{k',m'}|^2] + \mathbb{E}[|R^{DLC,Q}_{k',m'}|^2] = p_1 T^{11,t,1}_{k',m'} + p_1^2 T^{11,t,2}_{k',m'} + p_1^3 T^{11,t,3}_{k',m'}$, where $T^{11,t,1}_{k',m'}$, $T^{11,t,2}_{k',m'}$ and $T^{11,t,3}_{k',m'}$, after a straightforward manipulation, are expressed by

$$T^{11,t,1}_{k',m'} = |a_1|^2 \sum_{l_2=0}^{L_2-1}\sum_{n_1=0}^{MK-1}\sum_{n_2=0}^{MK-1} \sigma^2_{1,l_2} f_{m'}[n_1] f^*_{m'}[n_2] \Lambda^{l_2}_{n1,n2} \times \left(|g_{TX,d}g_{RX,d}|^2 e^{\frac{j2\pi(n_1-n_2)\epsilon}{K}} + |g_{TX,I}g_{RX,I}|^2 \times e^{\frac{-j2\pi(n_1-n_2)\epsilon}{K}} + |g_{TX,I}g_{RX,d}|^2 e^{\frac{j2\pi(n_1-n_2)(\epsilon-2k')}{K}} + |g_{TX,d}g_{RX,I}|^2 e^{\frac{-j2\pi(n_1-n_2)(\epsilon+2k')}{K}}\right) \times g_{m'}[n_1-l_2] g^*_{m'}[n_2-l_2], \quad (22)$$

$$T^{11,t,2}_{k',m'} = 4K\Re\left[a_1 a_3^*\right] \sum_{l_2=0}^{L_2-1}\sum_{n_1=0}^{MK-1}\sum_{n_2=0}^{MK-1} \sigma^2_{1,l_2} f_{m'}[n_1] f^*_{m'}[n_2] \Lambda^{l_2}_{n1,n2} \times \left(|g_{TX,d}g_{RX,d}|^2 e^{\frac{j2\pi(n_1-n_2)\epsilon}{K}} + |g_{TX,I}g_{RX,I}|^2 \times e^{\frac{-j2\pi(n_1-n_2)\epsilon}{K}} + |g_{TX,I}g_{RX,d}|^2 e^{\frac{j2\pi(n_1-n_2)(\epsilon-2k')}{K}} + |g_{TX,d}g_{RX,I}|^2 e^{\frac{-j2\pi(n_1-n_2)(\epsilon+2k')}{K}}\right) \times g_{m'}[n_1-l_2] g^*_{m'}[n_2-l_2]\gamma[n_1-l_2] \quad (23)$$

and

$$T^{11,t,3}_{k',m'} = 4K^2|a_3|^2 \sum_{l_2=0}^{L_2-1}\sum_{n_1=0}^{MK-1}\sum_{n_2=0}^{MK-1} \sigma^2_{1,l_2} f_{m'}[n_1] f^*_{m'}[n_2] \Lambda^{l_2}_{n1,n2} \times \Big(|g_{TX,d} g_{RX,d}|^2 e^{\frac{j2\pi(n_1-n_2)\epsilon}{K}} + |g_{TX,I} g_{RX,I}|^2 \times e^{\frac{-j2\pi(n_1-n_2)\epsilon}{K}} + |g_{TX,I} g_{RX,d}|^2 e^{\frac{j2\pi(n_1-n_2)(\epsilon-2k')}{K}} + |g_{TX,d} g_{RX,I}|^2 e^{\frac{-j2\pi(n_1-n_2)(\epsilon+2k')}{K}} \Big) g_{m'}[n_1-l_2] g^*_{m'}[n_2-l_2] \gamma[n_1-l_2]\gamma[n_2-l_2] \quad (24)$$

where $\Lambda^{l_2}_{n1,n2}$ is a single function for representing phase noise term given by

$$\Lambda^{l_2}_{n1,n2} = \mathbb{E}\Big[e^{j(\phi_{TX,1}[n_1-l_2]-\phi_{RX,1}[n_1]-\phi_{TX,1}[n_2-l_2]+\phi_{RX,1}[n_2])} \Big] = e^{-\frac{1}{2}\mathbb{E}\left[|\phi_{TX,1}[n_1-l_2]-\phi_{RX,1}[n_1]-\phi_{TX,1}[n_2-l_2]+\phi_{RX,1}[n_2]|^2\right]}. \quad (25)$$

After finding the power of active digital cancellation symbols in (22)-(24), we derive the power of residual SI. According to independency between $d^{RSI,1}_{k',m'}$ and $R^{DLC,I}_{k',m'} + R^{DLC,Q}_{k',m'}$ in (12), the power of residual SI, $d^{RSI,1}_{k',m'} = R^1_{k',m'} - R^{DLC,I}_{k',m'} - R^{DLC,Q}_{k',m'}$, is equal to $p^1_{k',m'} = p^{1,t}_{k',m'} - p^{11,s}_{k',m'}$, where $p^{1,t}_{k',m'} = [|R^1_{k',m'}|^2]$. Due to several cross terms that are equal to zero, we find that $p^{1,t}_{k',m'} = p_1 T^{1,t,1}_{k',m'} + p_1^2 T^{1,t,2}_{k',m'} + p_1^3 T^{1,t,3}_{k',m'}$, where by using output of active digital cancellation (12), $T^{1,t,1}_{k',m'}$, $T^{1,t,2}_{k',m'}$ and $T^{1,t,3}_{k',m'}$ are derived by

$$T^{1,t,1}_{k',m'} = K|a_1|^2 \sum_{l_2=0}^{L_2-1}\sum_{n=0}^{MK-1}\sum_{m_1,m_2=0}^{MK-1} \sigma^2_{1,l_2} f_{m'}[n] f_{(m'+m_1)_M}[n] \times \Lambda^{l_2}_{n,Kn+m_1} \Big(|g_{TX,d}|^2 + |g_{TX,I}|^2 \Big) \times \Big(|g_{RX,d}|^2 e^{\frac{j2\pi\epsilon(n-\zeta[n,m_1])}{K}} + |g_{RX,I}|^2 e^{-\frac{j2\pi\epsilon(n-\zeta[n,m_1])}{K}} \Big) \times g_{m_2}[n-l_2] g_{(m_2+m_1)_M}[n-l_2], \quad (26)$$

$$T^{1,t,2}_{k',m'} = 4K^2 \Re\big[a_1 a_3^*\big] \sum_{l_2=0}^{L_2-1}\sum_{n=0}^{MK-1}\sum_{m_1,m_2,m_3=0}^{MK-1} \sigma^2_{1,l_2} f_{m'}[n] \times f_{(m'+m_1)_M}[n] \Lambda^{l_2}_{n,Kn+m_1} \Big(|g_{TX,d}|^2 + |g_{TX,I}|^2 \Big) \times \Big(|g_{RX,d}|^2 e^{\frac{j2\pi\epsilon(n-\zeta[n,m_1])}{K}} + |g_{RX,I}|^2 e^{-\frac{j2\pi\epsilon(n-\zeta[n,m_1])}{K}} \Big) \times g_{m_2}[n-l_2] g_{(m_1+m_2)_M}[n-l_2] |g_{(m_1+m_3)_M}[n-l_2]|^2 \quad (27)$$

and

$$T^{1,t,3}_{k',m'} = K^3|a_3|^2 \sum_{l_2=0}^{L_2-1}\sum_{n=0}^{MK-1}\sum_{m_1,m_2,m_3,m_4=0}^{MK-1} \sigma^2_{1,l_2} f_{m'}[n] \times f_{(m'+m_1)_M}[n] \Lambda^{l_2}_{n,Kn+m_1} \Big(|g_{TX,d}|^2 + |g_{TX,I}|^2 \Big) \times \Big(|g_{RX,d}|^2 e^{\frac{j2\pi\epsilon(n-\zeta[n,m_1])}{K}} + |g_{RX,I}|^2 e^{-\frac{j2\pi\epsilon(n-\zeta[n,m_1])}{K}} \Big) \times g_{m_3}[n-l_2] g_{(m_3+m_1)_M}[n-l_2] g_{m_4}[n-l_2] g_{(m_1+m_2)_M} \times [n-l_2]\big(4 g_{m_4}[n-l_2] g_{(m_1+m_2)_M}[n-l_2] + 2 g_{m_2}[n-l_2] g_{(m_1+m_4)_M}[n-l_2]\big). \quad (28)$$

Now, we want to derive (25) for the two oscillator configurations.

1) TWO SEPARATE OSCILLATORS

Thus, the transmitter and receiver of SU_1 will have independent Brownian motion processes $\phi_{Tx,1}(t)$ and $\phi_{Rx,1}(t)$. Therefore, two phase noise difference terms $\phi_{TX,1}[n_1-l_2] - \phi_{TX,1}[n_2-l_2]$ and $\phi_{TX,1}[n_2] - \phi_{TX,1}[n_1]$ in (25) are mutually independent normal random variables. Then, by using the presented phase noise function in (15), (25) can be written as

$$\Lambda^{l_2,ind}_{n1,n2} = e^{-4|n_1-n_2|\pi\beta T_s}. \quad (29)$$

2) ONE COMMON SHARED OSCILLATOR

We now have $\phi_{Tx,1}(t) = \phi_{Rx,1}(t) = \phi_1(t)$. In this configuration, for every pair of n_1 and n_2 for every value of l_2, we should find two non-overlapped groups of the phase noise differences in time. According to the properties of Wiener processes, they will be independent, and we can use (15) to find (25). After several manipulations, (25) for the common oscillator case is derived as

$$\Lambda^{l_2,comm}_{n1,n2} = \begin{cases} e^{-4|n_1-n_2|\pi\beta T_s} & |n_1-n_2| < l_2 \\ e^{-4l_2\pi\beta T_s} & |n_1-n_2| \geq l_2. \end{cases} \quad (30)$$

By inserting (29) and (30) in (22)-(24) and (26)-(28), power of residual SI for the case of independent oscillator and common shared oscillator are derived, respectively. Obviously, derived expression in (22)-(24) and (26)-(28) is function of system parameters and can be derived for any arbitrary configurations.

D. POWER OF THERMAL NOISE

Next, we derive the power of equivalent noise components in (12). With additive Gaussian noise $n_1[n] \sim \mathcal{N}(0, \sigma_n^2)$, the variance of linear equivalent noise $w^{eq,I}_{k',m'}$ in (12) is given by

$$\sigma^{n,I}_{k',m'} = \mathbb{E}\Big[|w^{eq,I}_{k',m'}|^2\Big] = |g_{RX,d}|^2 \sigma_n^2 \sum_{n=0}^{MK-1} |f_{m'}[n]|^2. \quad (31)$$

Similarly, the power of conjugate equivalent noise $w^{eq,Q}_{k',m'}$ in (12) is written as

$$\sigma^{n,Q}_{k',m'} = \mathbb{E}\Big[|w^{eq,Q}_{k',m'}|^2\Big] = |g_{RX,I}|^2 \sigma_n^2 \sum_{n=0}^{MK-1} |f_{m'}[n]|^2. \quad (32)$$

Variances in (31) and (32) show that noise power depends on IQ imbalance coefficients, noise variance and the receiver filter. Thus, the total noise power can be written as $\sigma^n_{k',m'} = \sigma^{n,I}_{k',m'} + \sigma^{n,Q}_{k',m'}$.

E. SINR FORMULATION

Finally, following the (16)-(18), (22)-(24) and (26)-(28), (31) and (32), the SINR associated with the desired signal transmitted from SU_2 to SU_1 may be formulated as

$$\Gamma^{21}_{k',m'} = \frac{p^{2,s}_{k',m'}}{p^{21}_{k',m'} + p^{1}_{k',m'} + \sigma^{n}_{k',m'}} = \frac{\sum_{a=1}^{3} p_2^a T^{2,s,a}_{k',m'}}{\left(\sum_{a=1}^{3} p_2^a T^{21,s,a}_{k',m'} + p_1^a T^{11,s,a}_{k',m'}\right) + \sigma^{n}_{k',m'}} \quad (33)$$

where $T^{2,s,a}_{k',m'} = T^{21,t,a}_{k',m'} - T^{2,s,a}_{k',m'}$ and $T^{11,s,a}_{k',m'} = T^{1,t,a}_{k',m'} - T^{11,t,a}_{k',m'}$, $a = 1, 2, 3$. Clearly, (33) is a function of system parameters and specially average transmit power of SU_1, p_1 and that of SU_2, p_2.

IV. ACI DERIVATION

Here, we will assess the ACI, caused by out-of-band emission of the two full-duplex nodes SU_1 and SU_2, on the lower and upper neighboring PUs. To do that, recall that the channels between SU_i and lower and upper active PUs, $h_{l,i}$ and $h_{r,i}$, $i \in \{1, 2\}$, are frequency selective channels. We assume they are constant over each frequency bin in frequency domain. To derive ACI caused by SU_1, we first need to derive the PSD of the SU_1 transmitted output $y_1(t)$ in (6). By using the nonlinear PA output (3), the autocorrelation function of $y_1(t)$, $R_{y_1y_1}(t, \tau) = \mathbb{E}[y_1(t)y_1^*(t-\tau)]$, can be written as

$$R_{y_1y_1}(t, \tau) = e^{-2|\tau|\pi\beta T_s}\left(|g_{Tx,d}|^2 + |g_{Tx,I}|^2\right)R_{Z1,Z1}(t, \tau) \quad (34)$$

where $Z_1(t) = a_1x_1(t) + a_3x_{PA,1}(t)$ and $R_{Z_1Z_1}(t, \tau) = \mathbb{E}[Z_1(t)Z_1^*(t-\tau)]$. Reference [35] proved that $R_{Z_1Z_1}(t, \tau)$ is a cyclostationary process with the property of $R_{Z_1Z_1}(t, \tau) = R_{Z_1Z_1}(t + MT_s, \tau)$. By taking the expectation over one period, the average autocorrelation function can be derived $\bar{R}_{Z_1Z_1}(t, \tau)$. By taking its Fourier transform, the PSD of $Z_1(t)$ has been given as [35]

$$S_{Z_1Z_1}(f) = p_1\eta_1(f) + {p_1}^2\eta_2(f) + {p_1}^3\eta_3(f) \quad (35)$$

where $\eta_1(f)$, $\eta_2(f)$ and $\eta_3(f)$ are derived in [35] and are listed in the bottom of the page in (36).

In (36), $G_m(f)$ is the frequency response of each filter and operator $\otimes$ denotes convolution. All the details of the derivation are available in [35] and references therein. Thus, for brevity, we do not list them here. By taking Fourier transform of autocorrelation in (34) the PSD of $y_1(t)$ may be expressed by $S_{y_1y_1}(f) = p_1S_{1,1}(f) + p_1^2S_{1,2}(f) + p_1^3S_{1,3}(f)$, where $S_{1,1}(f)$, $S_{1,2}(f)$ and $S_{1,3}(f)$ may be written as

$$S_{1,i}(f) = \frac{4\pi\beta T_s\left(|g_{Tx,d}|^2 + |g_{Tx,I}|^2\right)}{(2\pi\beta T_s)^2 + 4\pi^2f^2} \otimes \eta_i(f), \quad i = 1, 2, 3. \quad (37)$$

By using the PSD of SU_1 transmit output $y_1(t)$ (37), the ACI generated by SU_1 on lower and upper channels can be derived as $P_{l,1} = p_1\psi_{l1,1} + p_1^2\psi_{l1,2} + p_1^3\psi_{l1,3}$ and $P_{r,1} = p_1\psi_{r1,1} + p_1^2\psi_{r1,2} + p_1^3\psi_{r1,3}$, respectively, where $\psi_{l,i}$ and $\psi_{r,i}$, $i = 1, 2, 3$, may be expressed as

$$\psi_{l1,i} = \sum_{d=K+1}^{2K} H_{l,1}(d-K)\int_{f_d-1/(2T_s)}^{f_d+1/(2T_s)} S_{1,i}(f)df$$
$$\psi_{r1,i} = \sum_{d=K+1}^{2K} H_{r,1}(d-K)\int_{-f_d-1/(2T_s)}^{-f_d+1/(2T_s)} S_{1,i}(f)df \quad (38)$$

where $f_d = \frac{K+2d+1}{2T_s}$, and $H_{l,1}(d)$ and $H_{r,1}(d)$ are channel gain of $h_{l,1}(t)$ and $h_{r,1}(t)$, respectively, in $d-$th frequency bin. Similarly, the ACI of SU_2 on the lower and upper channels could be derived. We omit the details for brevity.

V. SUM RATE MAXIMIZATION

We now formulate the maximization of the sum rate of the full-duplex link given the ACI constraints on lower and upper neighboring channels of the spectrum hole. By utilizing the derived SINR expression (33), we formulate the achievable rates of SU_1 and SU_2 as follows:

$$R^{21}(p_1, p_2) = \sum_{k'=0}^{K-1}\sum_{m'=0}^{M-1}\log_2\left(1 + \Gamma^{21}_{k',m'}\right)$$
$$R^{12}(p_1, p_2) = \sum_{k'=0}^{K-1}\sum_{m'=0}^{M-1}\log_2\left(1 + \Gamma^{12}_{k',m'}\right) \quad (39)$$

$$\eta_1(f) = \frac{|a_1|^2}{MT_s}\sum_{k=0}^{K-1}\sum_{m=0}^{M-1}\left|G_m\left(f - \frac{\left(k - \frac{K-1}{2}\right)}{T_s}\right)\right|^2$$
$$\eta_2(f) = 4\Re[a_1a_3^*]\frac{K}{MT_s}\left(\sum_{m=0}^{M-1}\sum_{m'=0}^{M-1}\left(G_m(f) \otimes |G_{m'}(f)|^2\right) \times G_m^*(f)\right) \otimes \sum_{k=0}^{K-1}\delta\left(f - \frac{k - \frac{K-1}{2}}{T_s}\right)$$
$$\eta_3(f) = \left(4|a_3|^2\frac{K^2}{MT_s}\left(\sum_{m=0}^{M-1}\sum_{m'=0}^{M-1}\sum_{m''=0}^{M-1}\left(G_m(f) \otimes |G_{m'}(f)|^2 \otimes \left|G_{m''}(f)\right|^2\right) \times G_m^*(f)\right) \otimes \sum_{k=0}^{K-1}\delta\left(f - \frac{k - \frac{K-1}{2}}{T_s}\right)\right)$$
$$+ \left(\begin{array}{l}\frac{2|a_3|^2}{MT_s}\left(\sum_{m=0}^{M-1}\sum_{m'=0}^{M-1}\sum_{m''=0}^{M-1}\left(G_m(f) \otimes G_{m'}(f) \otimes G_{m''}^*(-f)\right) \times \left(G_m^*(f) \otimes G_{m'}^*(f) \otimes G_{m''}(-f)\right)\right) \\ \otimes \sum_{k=0}^{K-1}\sum_{k'=0}^{K-1}\sum_{k''=0}^{K-1}\delta\left(f - \frac{k+k'-k''-\frac{K-1}{2}}{T_s}\right)\end{array}\right) \quad (36)$$

where these rates are specified in the units of bits/second per Hertz or bps/Hz. Note that rates of SU_1 and SU_2 depend on all the system parameters. Thus, these expressions allow for comparative performance evaluations of different parameter configurations. Moreover, impacts of RF impairments on the system performance can be qualified and measured, and thus design guidelines can be developed. By utilizing the ACI expressions (38) and the above rates (39), the sum-rate maximization problem may be formulated as

$$\max_{p_1,p_2} \; R^{21}(p_1,p_2)+R^{12}(p_1,p_2) \tag{40}$$

$$\begin{aligned} s.t.\;\; & p_1 \le P_{\max}, p_2 \le P_{\max}, \\ & \sum_{a=1}^{3} p_1^a \psi_{l1,a} < I_{l,max}, \qquad \sum_{a=1}^{3} p_1^a \psi_{r1,a} < I_{r,max}, \\ & \sum_{a=1}^{3} p_2^a \psi_{l2,a} < I_{l,max}, \qquad \sum_{a=1}^{3} p_2^a \psi_{r2,a} < I_{r,max} \end{aligned} \tag{41}$$

where P_{max} is the maximum allowable transmit power, $I_{l,max}$ and $I_{r,max}$ are the maximum tolerable interference power on the lower and upper PUs from each full-duplex node, respectively. The constraints force that the average transmit power of SU_1 and SU_2 should be lower than

$$\begin{aligned} p_1 < P'_{1,max} = \min\Bigg\{ & P_{\max}, root^{+}\Bigg(\sum_{a=1}^{3} p_1^a \psi_{l1,a} - I_{l,max}\Bigg), \\ & root^{+}\Bigg(\sum_{a=1}^{3} p_1^a \psi_{r1,a} - I_{r,max}\Bigg)\Bigg\} \\ p_2 < P'_{2,max} = \min\Bigg\{ & P_{\max}, root^{+}\Bigg(\sum_{a=1}^{3} p_2^a \psi_{l12,a} - I_{l,max}\Bigg), \\ & root^{+}\Bigg(\sum_{a=1}^{3} p_2^a \psi_{r2,a} - I_{r,max}\Bigg)\Bigg\} \end{aligned} \tag{42}$$

where $root^{+}(f(x))$ stands for the set of the real positive roots of $f(x)=0$. Because of the interference constraints, the problem (40) is not convex. Non-convex problems are in general very tough to handle. Thus, we use a series of successive convex approximations until convergence. To do that, we approximate the denominator and nominator of SINR with affine functions based on first-order Taylor series expansion as $f(x(t)) = f(x(t-1)) + f'(x(t-1))(x(t)-x(t-1))$, where t is the iteration index and $x(t-1)$ is the optimal solution of $t-1$ iteration [43]. Therefore, SINRs of SU_2 and SU_1 are approximated by

$$\begin{aligned} \tilde{\Gamma}^{21}_{k',m'}(t) &= \frac{A^2_{k',m'}(t-1)p_2(t) + E^2_{k',m'}(t-1)}{B^2_{k',m'}(t-1)p_2(t) + C^1_{k',m'}(t-1)p_1(t) + F^2_{k',m'}(t-1)} \\ \tilde{\Gamma}^{12}_{k',m'}(t) &= \frac{A^1_{k',m'}(t-1)p_1(t) + E^1_{k',m'}(t-1)}{B^1_{k',m'}(t-1)p_1(t) + C^2_{k',m'}(t-1)p_2(t) + F^1_{k',m'}(t-1)}. \end{aligned} \tag{43}$$

Proof: See Appendix E. ■

Now we can rewrite the sum rate optimization problem as

$$\max_{p_1,p_2} \; \sum_{k'=0}^{K-1}\sum_{m'=0}^{M-1} \log_2\Big(1+\tilde{\Gamma}^{21}_{k',m'}\Big) + \sum_{k'=0}^{K-1}\sum_{m'=0}^{M-1} \log_2\Big(1+\tilde{\Gamma}^{12}_{k',m'}\Big) \tag{44}$$

$$s.t.\;\; p_1 \le P'_{1,\max}, p_2 \le P'_{2,\max}. \tag{45}$$

We convert (44) into a minimization problem, and after that transform it to a logarithm of a multiplication terms as

$$\begin{aligned} \min_{p_1,p_2} \; & \log \prod_{k'=0}^{M-1}\prod_{m'=0}^{K-1} \Big(1+\tilde{\Gamma}^{21}_{k',m'}\Big)^{-1} \\ & + \log \prod_{k'=0}^{M-1}\prod_{m'=0}^{K-1} \Big(1+\tilde{\Gamma}^{12}_{k',m'}\Big)^{-1}. \end{aligned} \tag{46}$$

To write fractional terms of (46) in the form of posynomial functions, the arithmetic-geometric mean approximation (AGMA) can be used [37]. In this method, a fraction of two posynomial functions, $F(x) = \frac{\sum_{k=1}^{N_f} f_k(x)}{\sum_{i=1}^{N_g} g_i(x)}$, is converted to the posynomial function as

$$\tilde{F}(x(t)) = \sum_{k=1}^{N_f} f_k(x) \left(\prod_{i=1}^{N_g} \left(\frac{g_i(x(t))}{\eta_i(t)} \right)^{\eta_i(t)} \right) \tag{47}$$

where $\eta_i(t) = \frac{g_i(t-1)}{\sum_{i'=1}^{N_g} g_{i'}(t-1)}$. Therefore, by using the AGMA, two sum rate components in (46) are converted to (48). This equation is given in the bottom of the next page.

The optimal powers are given by

where the two delta terms in (48) are given by

$$\begin{aligned} \Delta_1(t) &= \Big(A^2_{k',m'}(t) + B^2_{k',m'}(t)\Big)p_2(t) + C^1_{k',m'}(t)p_1(t) \\ &\quad + E^2_{k',m'}(t) + F^2_{k',m'}(t) \\ \Delta_2(t) &= \Big(A^1_{k',m'}(t) + B^1_{k',m'}(t)\Big)p_1(t) + C^2_{k',m'}(t)p_2(t) \\ &\quad + E^1_{k',m'}(t) + F^1_{k',m'}(t). \end{aligned} \tag{49}$$

Since problem (48) is a standard geometric program (GP), Algorithm 1 can solve with the constraints of (45) by utilizing the CVX tool [37], which uses an interior point method. The number of iterations is $\frac{\log(c/t_0\beta)}{\log(\eta)}$, where c, t_0, $0<\beta<1$ and η are the number of constraints, the initial point to approximate the accuracy, the stopping criterion and the updating parameter, respectively. The computation required for the AGMA in each iteration in our problem is KM, and the total computational complexity is $KM\frac{\log(2/t_0\beta)}{\log(\eta)}$.

The full algorithm is given in Algorithm 1.

VI. SIMULATION RESULTS

Here, first, the residual SI powers for both cases of Case 1- two independent oscillators and Case 2- single shared oscillator in (25)-(30) are verified via simulation results. The following results are given for both GFDM and OFDM. First, the SINR expression (33) is computed. Second, the

Algorithm 1 Sum Rate Maximization Algorithm

1: Set the maximum number of iteration $I_{\max}$ and convergence condition ϱ.
2: Set $t \leftarrow 1$ and initialize $p_1(0) = p_2(0) = P_{max}$ and Calculate $\Delta_1(0)$ and $\Delta_2(0)$ by (49) .
3: **do while** $|p_1(t) - p_1(t-1)| \leq \varrho$ and $|p_2(t) - p_2(t-1)| \leq \varrho$ and $t < I_{\max}$
4: Derive $p_1(t)$ and $p_2(t)$ by solving (48) given constraints (45).
5: Update $\Delta_1(t)$ and $\Delta_2(t)$ by $p_1(t)$ and $p_2(t)$ by using (49).
6: $t \leftarrow t+1$ 7: **end do** 8: **return**

PSD of transmitted signal (37) is verified with simulation results and adjacent channel power ratio (ACPR). Third, the sum rate maximization of the full-duplex link (48) given PU interference constraints (45) is solved for several different scenarios.

A. SYSTEM MODELS AND PARAMETERS

1) GFDM AND OFDM

Note that GFDM includes OFDM as a special case. Thus, by setting $M = 1$, and prototype filter $g[n]$ equal to rectangular pulse shape, we get OFDM. Therefore, all the derived expressions can also be used for OFDM.

We use $K = 32$ subcarriers, $M = 5$ time-slots, root raised-cosine filter with the roll-off factor 0.1 and zero forcing receiver [31] for GFDM. OFDM also uses 32 subcarriers. Sampling time is equal to 100 ns [21] and the cyclic prefix for both GFDM and OFDM is equal to the length of the channel.

2) PA NON-LINEARITY

We consider linear and non-linear PAs: (1) linear, denoted by PA_1, with the polynomial coefficients $a_1 = 15.0008 + j0.0908$ and $a_3 = 0$ and, (2) nonlinear, denoted by PA_2 with $\{a_1, a_3 = -23.0826 + j3.3133\}$. Variance of the noise is 0 dB and maximum allowable power is equal to PA 1- dB compression point, $P_{max} = P_{1dB} = 23$ dBm, that is derived from [35].

3) CHANNEL MODELS

ITU outdoor channel model A is considered for generating multi-path components of $h_{21}(t) = h_{12}(t)$ with power delay profile of 0 dB, −1 dB, −9 dB, −10 dB, −15 dB and −20 dB for delays of 0, 3, 7, 11, 17 and 25 samples. Furthermore, The power delay profile of SI channel in [21] is utilized for $h_{11}(t) = h_{22}(t)$ which is 0 dB, −35 dB, −40 dB and −45 dB for delays of 0, 1, 2 and 4 samples. Moreover, interference channels between two nodes and PUs in lower and upper channels are generated from a 7-tap multipath model with exponential power profile $\sigma_i = \sum_{k=0}^{6} \exp(i-k)/2$, $i = 0, \ldots, 6$.

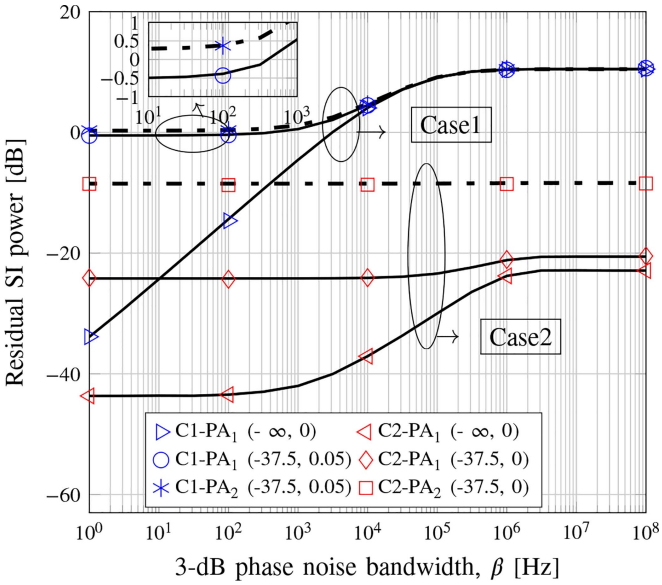

FIGURE 3. SU_1 residual SI power versus 3 dB phase noise bandwidth. Legends C1 and C2 denote Case 1 and Case 2, respectively.

Moreover, in Fig. 3-Fig. 7, simulation results are shown with markers. Moreover, theoretical results for linear PA_1 and nonlinear PA_2 are indicated with solid and dotted lines, respectively.

Note that GFDM with a linear PA has lower out-of-band emissions compared with OFDM. Moreover, this advantage is retained in the presence of nonlinear PA [35]. Moreover, GFDM offers flexible design of its prototype filter to further reduce out-of-band emissions [14]. However, digital predistortion [44] and crest factor reduction [45] techniques can be deployed for both GFDM and OFDM to reduce nonlinear interference. Since these techniques increase the complexity of the system, in this work, we compare conventional GFDM and OFDM only. However, digital pre-distorion and crest-factor reduction are potential future works.

$$\min_{p_1(t),p_2(t)} \prod_{k'=0}^{M-1}\prod_{m'=0}^{K-1}\Big(B^2_{k',m'}(t-1)p_2(t)+C^1_{k',m'}(t-1)p_1(t)+F^2_{k',m'}(t-1)\Big)\Big(B^1_{k',m'}(t-1)p_1(t)+C^2_{k',m'}(t-1)p_2(t)+F^1_{k',m'}(t-1)\Big)$$
$$\times(\Delta_1(t-1))^{-\frac{E^2_{k',m'}(t-1)+F^2_{k',m'}(t-1)}{\Delta_1(t-1)}}(\Delta_2(t-1))^{-\frac{E^1_{k',m'}(t-1)+F^1_{k',m'}(t-1)}{\Delta_2(t-1)}}\left(\frac{p_2(t)\Delta_1(t-1)}{p_2(t-1)}\right)^{-\frac{p_2(t-1)\left(A^2_{k',m'}+B^2_{k',m'}\right)}{\Delta_1(i-1)}}$$
$$\times\left(\frac{p_1(t)\Delta_2(t-1)}{p_1(t-1)}\right)^{-\frac{p_1(t-1)\left(A^1_{k',m'}+B^1_{k',m'}\right)}{\Delta_2(i-1)}}\left(\frac{p_1(t)\Delta_1(t-1)}{p_1(t-1)}\right)^{-\frac{p_1(t-1)C^1_{k',m'}}{\Delta_1(t-1)}}\left(\frac{p_2(t)\Delta_2(t-1)}{p_2(t-1)}\right)^{-\frac{p_2(t-1)C^2_{k',m'}}{\Delta_2(t-1)}} \quad (48)$$

To verify the accuracy of the derived expressions, we next plot our residual SI power analysis (25)-(30) and SINR (33) by simulation results. Furthermore, the SINRs of GFDM and OFDM are compared.

B. POWER ANALYSIS

Fig. 3 shows the SU_1 residual SI power in (25)-(30) versus 3-dB phase noise bandwidth for two cases; Case 1- two independent oscillators in (29) or Case 2 single shared oscillator (30). Node SU_1 uses $p_1 = 17$ dBm transmit power and GFDM. The set of IQ imbalance and CFO parameters are indicated by the legend (IRR [dB], ϵ).

To evaluate the system performance given the RF impairments, we investigate three scenarios for Case 1; 1) linear PA with no IQ imbalance and CFO (legend C1-PA_1 $(-\infty, 0)$), 2) linear PA with IQ imbalance and CFO (legend C1- PA_1 $(-37.5, 0.05)$), and 3) nonlinear PA with IQ imbalance and CFO (legend C1- PA_2 $(-37.5, 0.05)$). Similarly, aforementioned scenarios are considered for Case 2 with this exception that CFO is equal zero for all cases. The observations have been summarized as follows:

- We observe that, the simulation results for residual SI power fully match with the derived residual SI power in (25)-(30) for both Case 1 (29) and Case 2 (30).
- The promising finding is that residual SI power for Case 2 is significantly lower than that for Case 1 in all cases, e.g., when PA_1 $(-\infty, 0)$ and $\beta = 10$ kHz, Case 2 achieves 40 dB lower residual SI power. This due to the fact that Case 2 cancels more phase noise by receiver oscillator than Case 1. Furthermore, CFO disappears for Case 2, which decreases residual SI power, e.g., when PA_1 (-37.5,0.02) and $\beta = 10$ kHz, 30 dB is difference between two oscillator setups. Note that [21] demonstrated that Case2 is more beneficial for OFDM full-duplex transceivers given phase noise impairment. However, our results clearly confirm that Case 2 preserve its beneficial in the presence of other RF impairments and is a realistic scenario for compact GFDM and OFDM full-duplex transceivers.
- Moreover, since SU_1 average transmit power $p_1 = 17$ dBm is lower than $P_{1dB} = 23$ dBm, PA_2 works in linear region. Therefore, We expect that interference terms due to the nonlinearity are negligible and residual SI power for both PAs are equal. But, we observe that in Case 2, a gap exists between the nonlinear PA and the linear PA results, e.g., for Case 2 with $(-37.5, 0)$ and $\beta = 10$ kHz, 14 dB gap exists between PA_1 and PA_2. The reason is that receiver oscillator cannot perfectly eliminate the nonlinear PA terms. On the other hand, in Case 1, PA_1 achieves lower residual SI power than PA_2 but the gap between them is not as high as Case 2.

By using the derived residual SI power expressions (22)-(28), for illustrating impacts of RF impairments especially nonlinear PA on SI digital cancellation, we define active digital cancellation capability (G) as the ratio between residual SI power before and after active digital cancellation

$$G = \frac{1}{MK} \frac{\sum_{k'=0}^{K-1} \sum_{m'=0}^{M-1} p_{k',m'}^{1,t}}{\sum_{k'=0}^{K-1} \sum_{m'=0}^{M-1} p_{k',m'}^{1}}. \tag{50}$$

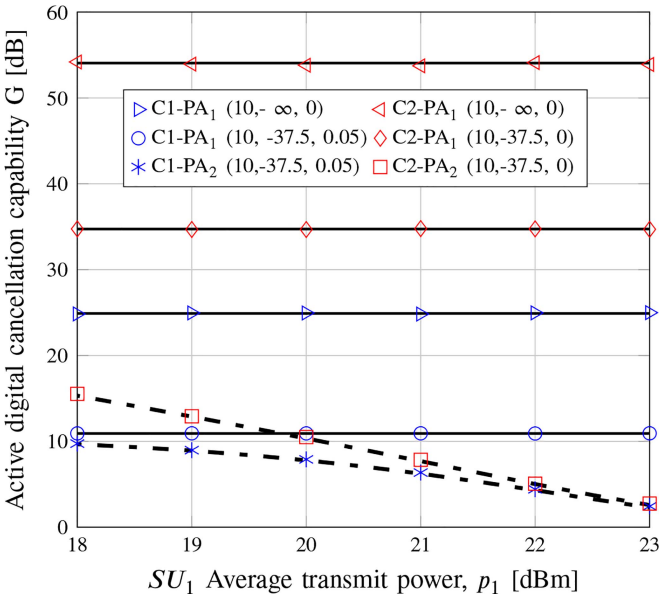

FIGURE 4. SU_1 active digital cancellation capability (50) versus SU_1 average transmit power, p_1.

Fig. 4 represents SU_1 active digital cancellation capability (G) in (50) versus average transmit power p_1 for the two oscillator setups. SU_1 uses GFDM. In this figure, the set of phase noise, IQ imbalance and CFO parameters are indicated by the legend (β [kHz], IRR [dB], ϵ). Three scenarios have been investigated for Case 1; 1) linear PA with phase noise (legend PA_1 $(10, -\infty, 0)$), 2) linear PA with phase noise, IQ imbalance and CFO (legend PA_1 $(10, -37.5, 0.05)$), and 3) nonlinear PA with phase noise, IQ imbalance and CFO (legend PA_2 $(10, -37.5, 0)$). Same scenarios are considered for Case 2 which CFO is equal to zero. The observations have been summarized as

- We observe that, with linear PA_1, G does not depend on the average transmit power. Thus, G remains constant for different transmit power levels. But this property does not hold for nonlinear PA_2. With increasing average transmit power approaching 23 dBm, active digital cancellation capability (G) decreases. Thus, with a nonlinear PA, nonlinear interference terms are not negligible and reduce the capability of active digital cancellation.
- Similar to Fig. 3, we observe that a single oscillator (Case 2) outperforms the use of two (Case 1) in terms of digital cancellation capability (G), e.g., when PA_1 $(10, -37.5, 0.05)$ with $p_1 = 21$ dBm, 20 dB is difference between the two oscillator setups. Furthermore, RF impairments reduce digital cancellation capability (G). Furthermore, since nonlinear interference terms are dominant in higher average transmit power, e.g., $p_1 = p_{1dB} = 23$ dBm, digital cancellation capabilities of

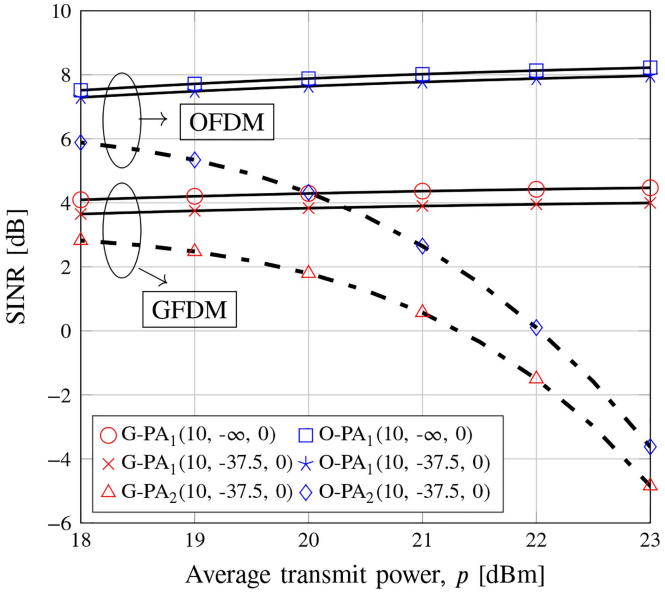

FIGURE 5. SINR vs average transmit power. SU_1 and SU_2 transmit at equal power levels, $p_1 = p_2 = p$. Legends "G" and "O" represent GFDM and OFDM.

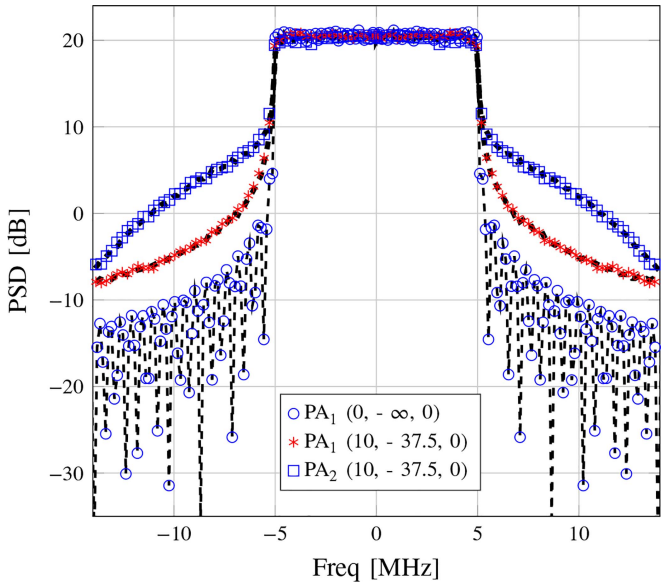

FIGURE 6. PSD of SU_1 output signal versus frequency.

these two oscillator setups converge to the same value. Thus, nonlinear PA plays a main role in decreasing the digital cancellation capability.

It is notable that Fig. 3 and Fig. 4 illustrate that the single oscillator (Case 2) outperforms the use of two (Case 1) in the presence of RF impairments. Thus, the single oscillator option is promising for full-duplex transceivers, and we deploy it exclusively for the remaining figures.

C. SINR ANALYSIS

Fig. 5 shows the SINR of SU_1 in (33) versus average transmit power. We assume that average transmit power of SU_1 and SU_2 are equal ($p_1 = p_2 = p$). Moreover, we assume that the parameters of RF impairments are the same for both nodes. Furthermore, SINR results for OFDM are presented. Three scenarios have been investigated for OFDM and GFDM; 1) linear PA with phase noise (legend $\text{PA}_1\ (10, -\infty, 0)$), 2) linear PA with phase noise and IQ imbalance (legend $\text{PA}_1\ (10, -37.5, 0)$), and 3) nonlinear PA with phase noise and IQ imbalance (legend $\text{PA}_2\ (10, -37.5, 0)$). Note that since Case 2 is utilized, CFO does not exist. Furthermore, we estimate the PSD via the averaged periodogram algorithm with 50% overlap and the Hanning window [30]. The observations of Fig. 5 have been summarized as follows:

- The theoretical (33) and simulated results match perfectly. This match verifies the accuracy of the derived expressions of desired symbol in (16)-(18), interference terms in (19)-(21) and thermal noise in (31) and (32).
- It is well known that GFDM confers the advantages of filter bank implementation and low peak-to-average power ratio [11]. Thus, we may expect that GFDM outperforms OFDM in terms of SINR. Unfortunately, this is not true, and we observe around 4 dB gap between OFDM and GFDM results. This is because non-orthogonality of GFDM causes more intercarrier interference and intersymbol interference terms and increases residual SI power. Furthermore, interference terms from SU_2 with GFDM is higher than OFDM. Therefore, SINR of the SU link using GFDM is lower than that using OFDM. However, for both OFDM and GFDM, the RF impairments reduce the SINR.
- We observe that, in all cases, when linear PA_1 is deployed, by increasing the average transmit power, SINR increases. The reason is that by increasing power, the effect of thermal noise in SINR (33) decreases. On the other hand, when nonlinear PA_2 is utilized, by increasing average transmit power and approaching to $p_{1dB} = 23$ dBm, SINR power monotonically decreases. It is due to the fact that nonlinear interference terms in nominator and denominator of SINR (33) are function of square and cube of power. Thus, in higher average transmit power, PA_2 works in nonlinear region and the interference terms are not negligible. In result, they reduce the power of desired terms and increase the power of interference and residual SI terms.

We next verify the derived PSD of transmitted signal from SU_1 in (37) by simulation results. Moreover, we compare the ACPR of GFDM and OFDM.

D. PSD ANALYSIS AND ACPR

In Fig. 6, PSD of transmitted signal from SU_1 in (37) is plotted versus the frequency in the presence of phase noise, IQ imbalance, and nonlinear PA. To show the effect of PA nonlinearity, we assume the average transmit power is equal to $p_1 = p_{sat} = 27$ dB (that is derived from [35]) and PAs operate in the nonlinear region. GFDM is deployed in the transmitter of SU_1. Three scenarios similar to the ones in

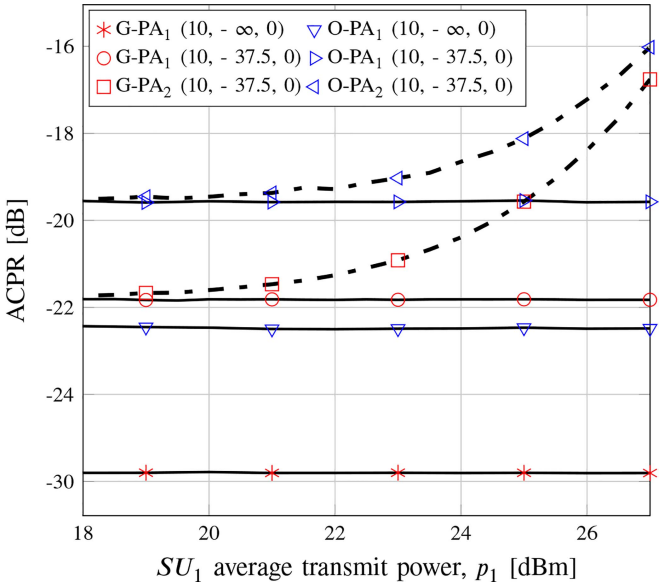

FIGURE 7. ACPR of SU_1 versus average transmit power of SU_1, p_1.

Fig. 5 are considered. The observations are summarized as follows:

- The simulation results verify the derived PSD of the transmit signal of SU_1 (37) in the presence of RF impairments.
- PSD is typically utilized to characterize broadband random signals and estimates the frequency content of the signal. PSD enables the evaluates in-band and out-of-band emissions (e.g., interference). Fig. 6 shows that RF impairments increase the out-of-band emission, increasing the interference on neighboring PUs. Especially, nonlinear PA causes spectrum regrowth due to out-of-band interference terms. These terms are function of square and cube of average transmit power and when the PA operates in the nonlinear region, their effects are much more severe, e.g., when $(10, -37.5, 0)$, out-of-band emission of PA_2 is -6 dB higher than PA_1.

By using PSD of SU_1 output signal (37), to show the impacts of RF impairments on the out-of-band emission, we define ACPR as

$$\zeta = \frac{\int_{B_1}^{B_2} S_{y_1 y_1}(f) df}{\int_{-B_1}^{B_1} S_{y_1 y_1}(f) df} \tag{51}$$

where $[B_1, B_2]$ is a frequency interval of upper adjacent channel and $[-B_1, B_1]$ is a frequency interval of the main channel. In Fig. 6, we set $B_1 = 5$ MHz and $B_2 = 15$ MHz.

We are interested in how out-of-band emissions depend on the multicarrier modulation format used by the transceivers. Thus, Fig. 7 plots the ACPR for GFDM and OFDM versus transmit power of SU_1. Three scenarios as per Fig. 5 are considered. The observations are summarized as follows.

- Because GFDM uses non-orthogonal subcarriers, we may expect that it has higher out-of-band emissions than OFDM. But we in fact find that GFDM achieves lower ACPR in all cases, e.g., when PA_1 $(10, -\infty, 0)$ and the transmit power of SU_1 is 21 dBm, ACPR of OFDM is approximately 7 dB higher than GFDM. The reason is that GFDM has a filter bank structure, which reduces the out-of-band emission. Although [11] confirmed this, the present work illustrates that GFDM preserves this advantage even in the presence of the RF impairments and thus has lower interference on neighboring PUs.
- As seen in Fig. 6, RF impairments including phase noise and IQ imbalance increase ACPR and out-of-band emission, e.g., when $p_1 = 21$ dBm, there is 8 dB gap between PA_1 $(10, -37.5, 0)$ and PA_1 $(10, -\infty, 0)$. Furthermore, the RF impairments decrease the gap between ACPR of OFDM and GFDM, e.g., at PA_1 $(10, -\infty, 0)$, the gap is 7 dB, whereas when PA_1 $(10, -37.5, 0)$, the gap is 2.3 dB.
- On the other hand, when linear PA is deployed, the ACPR is independent of average transmit power and the gaps between GFDM and OFDM results is constant. However, when nonlinear PA_2 is deployed, by approaching to PA 1- dB compression point, ACPR monotonically increases and out-of-band emission on neighboring channel boosts since the power of nonlinear terms increases. Moreover, by approaching to PA 1- dB compression point, the gap between GFDM and OFDM decreases.

While OFDM outperforms GFDM in terms higher SINR (Fig. 5), the converse holds from the perspective of out-of-band emissions (Fig. 7). The SINR impacts the secondary link rate while out-of-band emission translates into interference on neighboring PU channels, a critical problem in cognitive radio networks. In the next section, we investigate the trade-off between these two effects.

E. SUM RATE MAXIMIZATION

Fig. 8 represents the optimized sum rate of SU link in (48) under ACI constraints in (45). For comparative purposes, we also present the optimized sum rate results of full-duplex OFDM. Moreover, we assume that SU_1 and SU_2 are identical in the sense that they both have the same RF impairments. Furthermore, maximum tolerable interference on the lower and upper PUs is the same, $I_{l,max} = I_{r,max} = I_{th}$. Three scenarios as in Fig. 5 are considered for GFDM and OFDM. The observations are explained as follows:

- On one hand, when the maximum tolerable interference power is high, e.g., $I_{th} = 0$ dB, the ACI constraint is not dominant and since full-duplex OFDM has higher SINR, it achieves higher sum rate. On the other hand, when the maximum tolerable interference power is tight, full-duplex GFDM can achieve higher sum rate since it has lower out-of-band emissions than OFDM, e.g., when PA_1 $(10, -\infty, 0)$, at $I_{th} = -36$ dB, the optimized sum rate of full-duplex GFDM is more than double that of full-duplex OFDM. It is notable that the critical requirement for realizing SU link in the spectrum

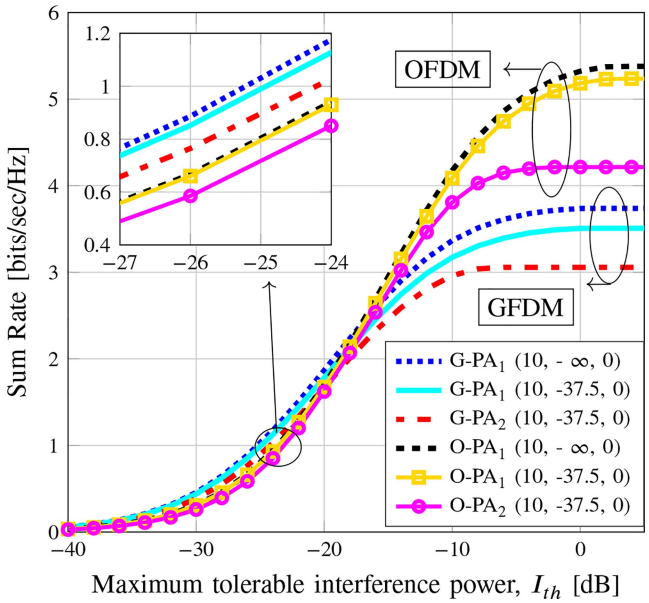

FIGURE 8. The optimized sum rate of SU link versus ACI constraint. Maximum tolerable interference power on the lower and upper PUs are same, $I_{l,max} = I_{r,max} = I_{th}$.

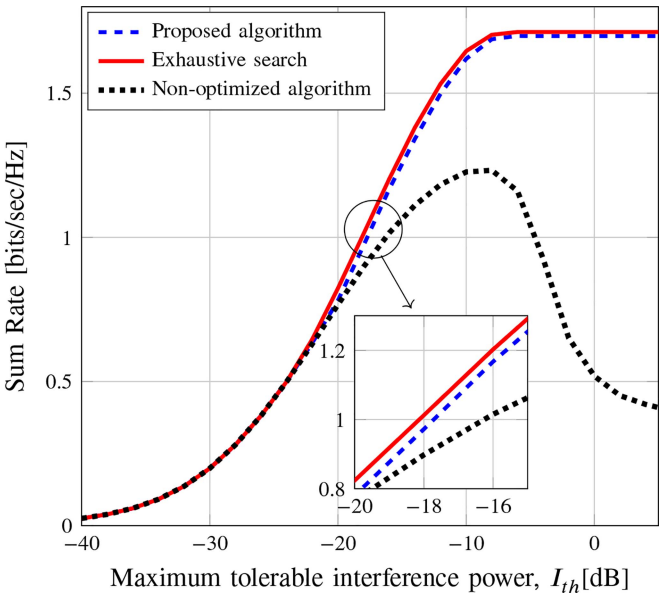

FIGURE 9. The optimized SU-link sum rate of versus ACI threshold for the different algorithms. The threshold is same for the lower and upper PU channels: $I_{l,max} = I_{r,max} = I_{th}$.

hole is low ACI on neighboring PUs. Thus, full-duplex GFDM, which has lower ACI, offers more data rates when exploiting the spectrum hole.

- However, RF impairments decrease the sum rate for GFDM and OFDM. For example, the when 3-dB phase noise bandwidth, IQ imbalance and CFO increase, the optimized sum rate in all cases decrease, due to increasing residual SI and intercarrier and intersymbol interference. Moreover, nonlinear PA$_2$ achieves lower sum rate in compared with linear PA$_1$, due to in-band and out-of-band nonlinear interference terms.

We next compare the performance of our proposed algorithm in (48) with two others: (1) Non-optimized algorithm; the transmit powers of SU_1 and SU_2 are set to maximum powers $P'_{1,max}$ and $P'_{2,max}$ in (42), respectively, and the sum rate in (40) is derived without any optimization and (2) Exhaustive search; the sum rate in (40) under ACI constraints in (45) is calculated for all possible SU_1 and SU_2 average transmit powers. For exhaustive search, we examine 10000×10000 (p_1,p_2) sets that are generated between zero and maximum powers $P'_{1,max}$ and $P'_{2,max}$ in (42). Moreover, we consider different RF impairments for SU_1 and SU_2 to understand how our proposed algorithm deals with different parameter configurations. The nonlinear PA$_2$ with phase noise 10 [kHz] are considered for both SU_1 and SU_2. The IQ imbalance of SU_2 and the receiver of SU_1 is equal to -37.5 [dB] and the only difference is the IQ imbalance of SU_1 transmitter which is equal to -17.5 [dB]. As can be seen, the proposed algorithm outperforms the non-optimized algorithm. On the other hand, the optimality gap (i.e., between the proposed algorithm and the exhaustive search), which is caused by approximation in (43), is almost negligible. Note that when the ACI threshold decreases, the optimality gap almost vanishes. This is because, smaller thresholds result in smaller transmit power allocations, and consequently, the impacts of nonlinear terms decrease. Thus, the error of the approximation in (43) is negligible.

VII. CONCLUSION

This paper has investigated the performance of full-duplex GFDM transceivers operating over a spectrum hole (whose lower and upper adjacent bands are PU active) in the presence of phase noise, IQ imbalance, CFO, and nonlinear PA. Both analog and digital SI cancellation techniques were considered and the residual SI power was derived for two cases - (1) two independent oscillators per transceiver and (2) single shared oscillator per transceiver. We also derived the powers of desired signal, interference signal and equivalent noise, SINR and the PSD. The power allocation was determined to maximize the sum rate of the secondary link. For this, we deployed a series of successive convex approximations to reach a standard geometric programming problem. Moreover, we showed that the gap between our proposed algorithm and an exhaustive search is negligible.

Some insights and implications of our findings are as follows.

1) Since simulation results fully match the derived analytical expressions, they have been validated. Thus, they may help us to quantify the tolerance of the system toward RF impairments and may also lead to RF circuit design guidelines and more.
2) In the presence of RF impairments, the single-shared oscillator setup significantly decreases the residual SI compared with that of two independent oscillators.

Thus, the single setup may be beneficial for up and down conversions in full-duplex transceivers.

3) Moreover, we extensively evaluated the impacts of RF impairments on a GFDM full-duplex link operating over a spectrum hole. The results show that RF impairments increase the residual SI power and out-of-band emissions. These results provide practical guidance for designing full-duplex GFDM links in secondary networks subject to interference constraints.
4) Finally, we find that the full-duplex GFDM link achieves significantly higher rates than the full-duplex OFDM link. For instance, the sum rate gains as high as 100% are sometimes achieved. Therefore, given RF impairments, GFDM is a potential candidate for realizing full-duplex links in secondary networks.

This paper focused on the ability of full-duplex GFDM transceivers to handle RF impairments and non-linear PA effects for a link over a spectrum hole. Cognitive and full-duplex radios offer a clear path for addressing the spectrum crunch. Hence, they offer invaluable developments for the emerging 5G and beyond wireless standards.

VIII. FUTURE RESEARCH TOPICS

This work can be extended in several directions. First, the assumption of perfect spectrum sensing may not hold in practical settings, and spectrum sensing errors will affect both the sum rate and interference levels on the primary users and also introduce primary interference on secondary receivers. These factors will then impact the throughput maximization of the secondary link. Spectrum sensing techniques include energy detection and others (see [46], [47] and references therein). The impacts of dynamic spectrum sensing and sensing errors for this system configuration are thus left for future research. Second, although relays are incorporated in both 4G and future wireless standards, the performance of full-duplex relays with RF impairments has not been reported thus far. This topic too is worthy of further study.

Moreover, a high peak-to-average-power ratio (PAPR) is a drawback of both GFDM and OFDM. PAPR of GFDM is studied in [14], [48], [49]. However, the impact of PAPR on GFDM full-duplex transceiver and appropriate reduction techniques are important research topics.

APPENDIX A
DESIRED SYMBOL

Based on the detected symbol model (11), the received signal from SU_2 can be written as a summation of desired symbol $d^{2,s}_{k',m'}$ and interference $d^{21}_{k',m'}$. Thus, we have

$$R^{21}_{k',m'} = \mu^{s}_{k',m'} d^{2}_{k',m'} + d^{21}_{k',m'} \tag{52}$$

where $d^{2,s}_{k',m'} = \mu^{s}_{k',m'} d^{2}_{k',m'}$. Since desired symbol and interference should be independent, we can derive $\mu^{s}_{k',m'}$ by $\mu^{s}_{k',m'} = \mathbb{E}[R^{21}_{k',m'} d^{*2}_{k',m'}]$. We defined that $R^{21}_{k',m'} = R^{21,I}_{k',m'} + R^{21,Q}_{k',m'} + R^{21,PA,I}_{k',m'} + R^{21,PA,Q}_{k',m'}$. Since complex data symbols are uncorrelated ($\mathbb{E}_d[d_{k_1,m_1} d^{*}_{k_2,m_2}] = \delta[k_1 - k_2]\delta[m_1 - m_2]$), $R^{21,Q}_{k',m'}$ and $R^{21,PA,Q}_{k',m'}$ are independent from $d^{*2}_{k',m'}$, $\mathbb{E}[R^{21,Q}_{k',m'} d^{*2}_{k',m'}] = \mathbb{E}[R^{21,PA,Q}_{k',m'} d^{*2}_{k',m'}] = 0$. Therefore, by using discrete GFDM signal in (1) and expressions in (9)-(11), we have that

$$\begin{aligned}\mu^{s}_{k',m'} &= \mathbb{E}\Big[(R^{21,I}_{k',m'} + R^{21,PA,I}_{k',m'}) d^{*2}_{k',m'}\Big] \\ &= \sum_{l_1=0}^{L_1-1} \sum_{n=0}^{MK-1} h^{I}_{21}[n, l_1] \Big(a_1 \mathbb{E}\Big[x_2[n-l_1] d^{*2}_{k',m'}\Big] \\ &\qquad + a_3 \mathbb{E}\Big[x_{PA,2}[n-l_1] d^{*2}_{k',m'}\Big]\Big) \\ &\qquad \times f_{m'}[n] e^{\frac{-j2\pi k' n}{K}}\end{aligned} \tag{53}$$

where $\mathbb{E}[x_2[n-l_1] d^{*2}_{k',m'}]$ is derived as

$$\mathbb{E}\Big[x_2[n-l_1] d^{*2}_{k',m'}\Big] = \sqrt{p_2} g_{m'}[n-l_1] e^{\frac{j2\pi k'(n-l_1)}{K}}. \tag{54}$$

Moreover, according to that $x_{PA,2}[n-l_1] = x_2[n-l_1]|x_2[n-l_1]|^2$, $\mathbb{E}[x_{PA,2}[n-l_1] d^{*2}_{k',m'}]$ is derived as

$$\begin{aligned}&\mathbb{E}\Big[x_{2,PA}[n-l_1] d^{*2}_{k',m'}\Big] \\ &= \sum_{k_1,k_2,k_3=0}^{K-1} \sum_{m_1,m_2,m_3=0}^{M-1} \mathbb{E}\Big[d^{1}_{k_1,m_1} d^{1}_{k_2,m_2} d^{*1}_{k_3,m_3} d^{*1}_{k',m'}\Big] \\ &\quad \times g_{m_1}[n-l_1] g_{m_2}[n-l_1] g^{*}_{m_3}[n-l_1] e^{j2\pi \frac{k1+k2-k3}{K}(n-l_1)}.\end{aligned} \tag{55}$$

Since complex data symbols are uncorrelated ($\mathbb{E}_d[d_{k_1,m_1} d^{*}_{k_2,m_2}] = \delta[k_1 - k_2]\delta[m_1 - m_2]$), for solving (55), we should consider two cases; 1) $k_1 = k_3$, $m_1 = m_3$, $k_2 = k'$, $m_2 = m'$, and 2) $k_1 = k'$, $m_1 = m'$, $k_2 = k_3$, $m_2 = m_2$. Thus, by calculating these two cases and after straightforward manipulation, (55) is simplified as

$$\begin{aligned}\mathbb{E}\Big[x_{2,PA}[n-l_1] d^{*2}_{k',m'}\Big] &= 2p_2\sqrt{p_2} K e^{\frac{j2\pi k'(n-l_1)}{K}} g_{m'}[n-l_1] \\ &\quad \times \sum_{m=0}^{M-1} |g_m[n-l_1]|^2.\end{aligned} \tag{56}$$

Therefore, by substituting (54) and (56) in (53), $\mu^{s}_{k',m'}$ is derived. In result, $d^{2,s}_{k',m'} = \mu^{s}_{k',m'} d^{2}_{k',m'}$ is derived in (13).

APPENDIX B
DIGITAL CANCELLATION SYMBOLS

By using detected symbol in (11), residual SI signal after active digital cancellation can be derived as

$$d^{RSI,1}_{k',m'} = R^{1}_{k',m'} - \mu^{I}_{k',m'} d^{1}_{k',m'} - \mu^{Q}_{k',m'} d^{*1}_{k',m'} \tag{57}$$

where $R^{DLC,I}_{k',m'} = \mu^{I}_{k',m'} d^{1}_{k',m'}$ and $R^{DLC,Q}_{k',m'} = \mu^{Q}_{k',m'} d^{*1}_{k',m'}$. Since linear and conjugate active digital cancellation symbols should be independent from each other and also $d^{RSI,1}_{k',m'}$, we can derive $\mu^{I}_{k',m'}$ and $\mu^{Q}_{k',m'}$ by $\mu^{I}_{k',m'} = \mathbb{E}[R^{1}_{k',m'} d^{*1}_{k',m'}]$ and $\mu^{Q}_{k',m'} = \mathbb{E}[R^{1}_{k',m'} d^{1}_{k',m'}]$, respectively. Similar to Appendix A and using discrete GFDM signal in (1) and expressions in (9)-(11), $\mu^{I}_{k',m'}$ and $\mu^{Q}_{k',m'}$ and in result $R^{DLC,I}_{k',m'} = \mu^{I}_{k',m'} d^{1}_{k',m'}$ and $R^{DLC,Q}_{k',m'} = \mu^{Q}_{k',m'} d^{*1}_{k',m'}$ can be derived. We omit the details for brevity.

APPENDIX C
POWER OF THE DESIRED SYMBOL

By using desired symbol in (13), $p^{2,s}_{k',m'} = \mathbb{E}[|d^{2,s}_{k',m'}|^2]$ can be written as

$$p^{2,s}_{k',m'} = \mathbb{E}\Big[|d^{2,s}_{k',m'}|^2\Big] = p_2\mathbb{E}\Big[d^2_{k',m'}d^{*2}_{k',m'}\Big]\sum_{l_1,l_3=0}^{L_1-1}\sum_{n_1,n_2=0}^{MK-1} \times \mathbb{E}\Big[h^I_{21}[n_1,l_1]h^{*I}_{21}[n_2,l_3]\Big](a_1+2Ka_3p_2\gamma[n_1-l_1]) \times \big(a^*_1+2Ka^*_3p_2\gamma[n_2-l_3]\big)f_{m'}[n_1]f^*_{m'}[n_2] \times g_{m'}[n_1-l_1]g^*_{m'}[n_2-l_3]. \quad (58)$$

We know that $\mathbb{E}[d^2_{k',m'}d^{*2}_{k',m'}] = 1$. Moreover, by considering the autocorrelation of phase noise in (15) and also $\mathbb{E}[|h_{21,l_1}|^2] = \sigma^2_{21,l_1}$, $l_1 = 0,1,\ldots,L_1-1$, $\mathbb{E}[h^I_{21}[n_1,l_1]h^{*I}_{21}[n_2,l_3]]$ can be derived as

$$\mathbb{E}\Big[h^I_{21}[n_1,l_1]h^{*I}_{21}[n_2,l_3]\Big] = \sigma^2_{21,l_1}e^{-4|n_1-n_2|\pi\beta T_s}\Big(|g_{TX,d}g_{RX,d}|^2e^{\frac{j2\pi(n_1-n_2)\epsilon}{K}} + |g_{TX,I}g_{RX,I}|^2e^{\frac{-j2\pi(n_1-n_2)\epsilon}{K}}\Big)\delta[l_1-l_3]. \quad (59)$$

Therefore, by substituting (59) in (58), $p^{2,s}_{k',m'}$ can be derived. Furthermore, $p^{2,s}_{k',m'}$ can be written as a summation of three terms as $p^{2,s}_{k',m'} = p_2T^{2,s,1}_{k',m'} + p_2^2T^{2,s,2}_{k',m'} + p_2^3T^{2,s,3}_{k',m'}$ in (16)-(18).

APPENDIX D
POWER OF INTERFERENCE TERMS

By using detected symbol in (11), we rewrite $R^{21}_{k',m'}$ as $R^{21}_{k',m'} = \chi^1_{k',m'} + \chi^2_{k',m'}$, where

$$\chi^1_{k',m'} = \sum_{l_1=0}^{L_1-1}\sum_{n=0}^{M-1} a_1\Big(h^I_{21}[n,l_1]x_2[n-l_1] + h^Q_{21}[n,l_1] \times x^*_2[n-l_1]\Big)f_{m'}[n]e^{-j2\pi\frac{k'}{K}n}$$

$$\chi^2_{k',m'} = \sum_{l_1=0}^{L_1-1}\sum_{n=0}^{M-1} a_3\Big(h^I_{21}[n,l_1]x_{PA,2}[n-l_1] + h^Q_{21}[n,l_1] \times x^*_{PA,2}[n-l_1]\Big)f_{m'}[n]e^{-j2\pi\frac{k'}{K}n}. \quad (60)$$

Now, $p^{21,t}_{k',m'} = [|R^{21}_{k',m'}|^2]$ is equal to

$$p^{21,t}_{k',m'} = \mathbb{E}\Big[|\chi^1_{k',m'}|^2\Big] + 2\Re\Big[\mathbb{E}\Big[\chi^1_{k',m'}\chi^{*2}_{k',m'}\Big]\Big] + \mathbb{E}\Big[|\chi^2_{k',m'}|^2\Big]. \quad (61)$$

Now we derive each component.

A. $\mathbb{E}[|\chi^1_{K',M'}|^2]$ DERIVATION

According to (60) and this fact that $\mathbb{E}[x_2[n_1-l_1]x^*_2[n_2-l_3]] = \mathbb{E}[x^*_2[n_1-l_1]x_2[n_2-l_3]]$, $\mathbb{E}[|\chi^1_{k',m'}|^2]$ can be formulated as

$$\mathbb{E}\Big[|\chi^1_{k',m'}|^2\Big] = |a_1|^2\sum_{l_1,l_3=0}^{L_1-1}\sum_{n_1,n_2=0}^{M-1}\Big(\mathbb{E}\Big[h^I_{21}[n_1,l_1]h^{*I}_{21}[n_2,l_3]\Big] + \mathbb{E}\Big[h^Q_{21}[n_1,l_1]h^{*Q}_{21}[n_2,l_3]\Big]\Big) \times \mathbb{E}\big[x_2[n_1-l_1]x^*_2[n_2-l_3]\big] \times f_{m'}[n_1]f^*_{m'}[n_1]e^{-j2\pi\frac{k'}{K}[n_1-n_2]}. \quad (62)$$

Like as $\mathbb{E}[h^I_{21}[n_1,l_1]h^{*I}_{21}[n_2,l_3]]$ derivation in (59), $\mathbb{E}[h^Q_{21}[n_1,l_1]h^{*Q}_{21}[n_2,l_3]]$ is derived. The summation of these two terms can be summarized as

$$\mathbb{E}\Big[h^I_{21}[n_1,l_1]h^{*I}_{21}[n_2,l_3]\Big] + \mathbb{E}\Big[h^Q_{21}[n_1,l_1]h^{*Q}_{21}[n_2,l_3]\Big] = \sigma^2_{21,l_1}e^{-4|n_1-n_2|\pi\beta T_s}\Big(|g_{TX,d}|^2 + |g_{TX,I}|^2\Big) \times \Big(|g_{RX,d}|^2e^{\frac{j2\pi(n_1-n_2)\epsilon}{K}} + |g_{RX,I}|^2e^{\frac{-j2\pi(n_1-n_2)\epsilon}{K}}\Big)\delta[l_1-l_3]. \quad (63)$$

On the other hand, $\mathbb{E}[x_2[n_1-l_1]x^*_2[n_2-l_3]]$ can be derived as

$$\mathbb{E}\big[x_2[n_1-l_1]x^*_2[n_2-l_3]\big] = p_1\sum_{k=0}^{K-1}\sum_{m=0}^{M-1} g_m[n_1-l_1] \times g^*_m[n_2-l_3]e^{j2\pi\frac{n_1-n_2}{K}k}. \quad (64)$$

Now by substituting (63) and (64) into (62), $\mathbb{E}[|\chi^1_{k',m'}|^2]$ can be derived. To reduce complexity, we deploy $\sum_{k=0}^{K-1}e^{-j2\pi\frac{k(n_1-n_2)}{K}} = K\sum_{t=0}^{M-1}\delta(n_1-n_2-tK)$. Final derivation can be presented by $\mathbb{E}[|\chi^1_{k',m'}|^2] = p_2T^{21,t,1}_{k',m'}$, where $T^{21,t,1}_{k',m'}$ is given in (19).

B. $\mathbb{E}[\chi^1_{K',M'}\chi^{*2}_{K',M'}]$ DERIVATION

According to that $\mathbb{E}[h_{21,l_1}h_{21,l_3}] = 0$, It can be easily shown that $\mathbb{E}[h^I_{21}[n_1,l_1]h^{*Q}_{21}[n_2,l_3]] = 0$. Therefore, according to (60), $\mathbb{E}[\chi^1_{k',m'}\chi^{*2}_{k',m'}]$ can be derived as

$$\mathbb{E}\Big[\chi^1_{k',m'}\chi^{*2}_{k',m'}\Big] = a_1a^*_3\sum_{l_1,l_3=0}^{L_1-1}\sum_{n_1,n_2=0}^{M-1} \times \Big(\mathbb{E}\Big[h^I_{21}[n_1,l_1]h^{*I}_{21}[n_2,l_3]\Big] + \mathbb{E}\Big[h^Q_{21}[n_1,l_1]h^{*Q}_{21}[n_2,l_3]\Big]\Big) \times \mathbb{E}\big[x_2[n_1-l_1]x^*_{PA,2}[n_2-l_3]\big] \times f_{m'}[n_1]f^*_{m'}[n_1]e^{-j2\pi\frac{k'}{K}[n_1-n_2]}. \quad (65)$$

By considering different cases like as what we have done in (56) and utilizing the mentioned equality for deriving $\mathbb{E}[|\chi^1_{k',m'}|^2]$, $\mathbb{E}[x_2[n_1-l_1]x^*_{PA,2}[n_2-l_3]]$ can be derived. Details are omitted for brevity. Therefore, by using derivations in (63) and (65), the final derivation is expressed as $2\Re[E[\chi^1_{k',m'}\chi^{*2}_{k',m'}]] = p_2^2T^{21,t,2}_{k',m'}$, where $T^{21,t,2}_{k',m'}$ is presented in (20).

C. $\mathbb{E}[|\chi^2_{k',M'}|^2]$ DERIVATION

Like as two previous subsections, $\mathbb{E}[\chi^1_{k',m'}\chi^{*2}_{k',m'}]$ can be written as

$$\begin{aligned}\mathbb{E}\Big[|\chi^1_{k',m'}|^2\Big] = |a_3|^2 \sum_{l_1,l_3=0}^{L_1-1}\sum_{n_1,n_2=0}^{M-1} &\times \Big(\mathbb{E}\Big[h^I_{21}[n_1,l_1]h^{*I}_{21}[n_2,l_3]\Big] \\ &+ \mathbb{E}\Big[h^Q_{21}[n_1,l_1]h^{*Q}_{21}[n_2,l_3]\Big]\Big) \\ &\times \mathbb{E}\big[x_{PA,2}[n_1-l_1]x^*_{PA,2}[n_2-l_3]\big] \\ &\times f_{m'}[n_1]f^*_{m'}[n_1]e^{-j2\pi\frac{k'}{K}[n_1-n_2]}. \end{aligned} \tag{66}$$

$\mathbb{E}[x_{PA,2}[n_1-l_1]x^*_{PA,2}[n_2-l_3]]$ is derived in [35]. By using derivations in (63) and (66), $\mathbb{E}[|\chi^2_{k',m'}|^2] = p_1^3 T^{1,t,3}_{k',m'}$, where $T^{1,t,3}_{k',m'}$ is presented in (21)

APPENDIX E
PROOF OF (43)

We write the SINR of desired signal transmitted from SU_2 to SU_1 (33) at t iteration as $\Gamma^{21}_{k',m'}(t) = F(p_2(t))/G(p_2(t),p_1(t))$, where $F(p_2(t)) = \sum_{a=1}^3 p_2^a(t)T^{2,s,a}_{k',m'}$ and $G(p_2(t),p_1(t)) = (\sum_{a=1}^3 p_2^a(t)T^{21,s,a}_{k',m'} + p_1^a(t)T^{11,s,a}_{k',m'}) + \sigma^n_{k',m'}$. Now, we calculate the approximation of $F(p_2(t))$ and $G(p_2(t),p_1(t))$ with affine functions at points $p_2(t-1)$ and $p_1(t-1)$ as $\tilde{F}(p_2(t)) = F(p_2(t-1)) + \frac{\partial F}{\partial p_2}(p_2(t-1))(p_2(t)-p_2(t-1))$ and $\tilde{G}(p_2(t),p_1(t)) = G(p_2(t-1),p_1(t-1)) + \frac{\partial G}{\partial p_2}(p_2(t-1))(p_2(t)-p_2(t-1)) + \frac{\partial G}{\partial p_1}(p_1(t-1))(p_1(t)-p_1(t-1))$. Therfeore, $\tilde{\Gamma}^{21}_{k',m'}(t) = \tilde{F}(p_2(t))/\tilde{G}(p_2(t),p_1(t))$. The final approximated $\tilde{\Gamma}^{21}_{k',m'}(t)$ is presented in (43), where

$$A^2_{k',m'}(t-1) = \sum_{a=1}^3 a p_2^{a-1}(t-1)T^{2,s,a}_{k',m'}$$

$$B^2_{k',m'}(t-1) = \sum_{a=1}^3 a p_2^{a-1}(t-1)T^{21,s,a}_{k',m'}$$

$$C^1_{k',m'}(t-1) = \sum_{a=1}^3 a p_1^{a-1}(t-1)T^{11,s,a}_{k',m'}$$

$$E^2_{k',m'}(t-1) = -\sum_{a=2}^3 (a-1)p_2^a(t-1)T^{2,s,a}_{k',m'}$$

$$F^2_{k',m'}(t-1) = -\Bigg(\sum_{a=2}^3 (a-1)\Big(p_2^a(t-1)T^{21,s,a}_{k',m'} + p_1^a(t-1) \times T^{11,s,a}_{k',m'}\Big)\Bigg) + \sigma^n_{k',m'}. \tag{67}$$

Similarly, $\tilde{\Gamma}^{12}_{k',m'}(t)$ in (43) can be calculated. Similar to (67), $A^1_{k',m'}(t-1)$, $B^1_{k',m'}(t-1)$, $C^2_{k',m'}(t-1)$, $E^1_{k',m'}(t-1)$, and $F^1_{k',m'}(t-1)$ are derived.

REFERENCES

[1] X. Dai, Z. Zhang, B. Bai, S. Chen, and S. Sun, "Pattern division multiple access: A new multiple access technology for 5G," *IEEE Wireless Commun.*, vol. 25, no. 2, pp. 54–60, Apr. 2018.

[2] M. Shafi *et al.*, "5G: A tutorial overview of standards, trials, challenges, deployment, and practice," *IEEE J. Sel. Areas Commun.*, vol. 35, no. 6, pp. 1201–1221, Jun. 2017.

[3] C. Wang *et al.*, "Cellular architecture and key technologies for 5G wireless communication networks," *IEEE Commun. Mag.*, vol. 52, no. 2, pp. 122–130, Feb. 2014.

[4] Z. Zhang, K. Long, A. V. Vasilakos, and L. Hanzo, "Full-duplex wireless communications: Challenges, solutions, and future research directions," *Proc. IEEE*, vol. 104, no. 7, pp. 1369–1409, Jul. 2016.

[5] M. Mohammadi, H. A. Suraweera, and C. Tellambura, "Uplink/downlink rate analysis and impact of power allocation for full-duplex cloud-RANs," *IEEE Trans. Wireless Commun.*, vol. 17, no. 9, pp. 5774–5788, Sep. 2018.

[6] Y. Liu, P. Roblin, X. Quan, W. Pan, S. Shao, and Y. Tang, "A full-duplex transceiver with two-stage analog cancellations for multipath self-interference," *IEEE Trans. Microw. Theory Techn.*, vol. 65, no. 12, pp. 5263–5273, Dec. 2017.

[7] Q. Cui, Y. Zhang, W. Ni, M. Valkama, and R. Jäntti "Energy efficiency maximization of full-duplex two-way relay with non-ideal power amplifiers and non-negligible circuit power," *IEEE Trans. Wireless Commun.*, vol. 16, no. 9, pp. 6264–6278, Sep. 2017.

[8] Y. Wang, W. Chen, and C. Tellambura, "Genetic algorithm based nearly optimal peak reduction tone set selection for adaptive amplitude clipping PAPR reduction," *IEEE Trans. Broadcast.*, vol. 58, no. 3, pp. 462–471, Sep. 2012.

[9] K. Sathananthan and C. Tellambura, "Coding to reduce both PAR and PICR of an OFDM signal," *IEEE Commun. Lett.*, vol. 6, no. 8, pp. 316–318, Aug. 2002.

[10] J. Jeong, Y. Park, S. Weon, J. Kim, S. Choi, and D. Hong, "Eigendecomposition-based GFDM for interference-free data transmission and pilot insertion for channel estimation," *IEEE Trans. Wireless Commun.*, vol. 17, no. 10, pp. 6931–6943, Oct. 2018.

[11] N. Michailow *et al.*, "Generalized frequency division multiplexing for 5th generation cellular networks," *IEEE Trans. Commun.*, vol. 62, no. 9, pp. 3045–3061, Sep. 2014.

[12] Z. Wang, L. Mei, X. Sha, and V. C. M. Leung, "Minimum BER power allocation for space-time coded generalized frequency division multiplexing systems," *IEEE Wireless Commun. Lett.*, vol. 8, no. 3, pp. 717–720, Jun. 2019.

[13] F. Li, K. Zheng, L. Zhao, H. Zhao, and Y. Li, "Design and performance of a novel interference-free GFDM transceiver with dual filter," *IEEE Trans. Veh. Technol.*, vol. 68, no. 5, pp. 4695–4706, May 2019.

[14] K. Liu, W. Deng, and Y. Liu, "Theoretical analysis of the peak-to-average power ratio and optimal pulse shaping filter design for GFDM systems," *IEEE Trans. Signal Process.*, vol. 67, no. 13, pp. 3455–3470, Jul. 2019.

[15] Z. Na, J. Lv, F. Jiang, M. Xiong, and N. Zhao, "Joint subcarrier and subsymbol allocation-based simultaneous wireless information and power transfer for multiuser GFDM in IoT," *IEEE Internet Things J.*, vol. 6, no. 4, pp. 5999–6006, Aug. 2019.

[16] S. Ehsanfar, M. Matthé, M. Chafii, and G. P. Fettweis, "Pilot- and CP-aided channel estimation in MIMO non-orthogonal multi-carriers," *IEEE Trans. Wireless Commun.*, vol. 18, no. 1, pp. 650–664, Jan. 2019.

[17] M. Amjad, F. Akhtar, M. H. Rehmani, M. Reisslein, and T. Umer, "Full-duplex communication in cognitive radio networks: A survey," *IEEE Commun. Surveys Tuts.*, vol. 19, no. 4, pp. 2158–2191, 4th Quart., 2017.

[18] W. Wang and H. Zhang, "Slotted secondary transmission with adaptive modulation and coding under interweave cognitive radio," *IEEE Trans. Veh. Technol.*, vol. 68, no. 5, pp. 4800–4809, May 2019.

[19] A. Mohammadian, M. Baghani, and C. Tellambura, "Analysis and rate optimization of GFDM-based cognitive radios," *Trans. Emerg. Telecommun. Technol.*, vol. 29, no. 9, p. e3435, 2019.

[20] D. Kim, H. Lee, and D. Hong, "A survey of in-band full-duplex transmission: From the perspective of PHY and MAC layers," *IEEE Commun. Surveys Tuts.*, vol. 17, no. 4, pp. 2017–2046, 4th Quart., 2015.

[21] V. Syrjälä, M. Valkama, L. Anttila, T. Riihonen, and D. Korpi, "Analysis of oscillator phase-noise effects on self-interference cancellation in full-duplex OFDM radio transceivers," *IEEE Trans. Wireless Commun.*, vol. 13, no. 6, pp. 2977–2990, Jun. 2014.
[22] X. Quan, Y. Liu, S. Shao, C. Huang, and Y. Tang, "Impacts of phase noise on digital self-interference cancellation in full-duplex communications," *IEEE Trans. Signal Process.*, vol. 65, no. 7, pp. 1881–1893, Apr. 2017.
[23] F. Shu, J. Wang, J. Li, R. Chen, and W. Chen, "Pilot optimization, channel estimation, and optimal detection for full-duplex OFDM systems with IQ imbalances," *IEEE Trans. Veh. Technol.*, vol. 66, no. 8, pp. 6993–7009, Aug. 2017.
[24] L. Samara, M. Mokhtar, O. Özdemir, R. Hamila, and T. Khattab, "Residual self-interference analysis for full-duplex OFDM transceivers under phase noise and I/Q imbalance," *IEEE Commun. Lett.*, vol. 21, no. 2, pp. 314–317, Feb. 2017.
[25] S. Li and R. D. Murch, "An investigation into baseband techniques for single-channel full-duplex wireless communication systems," *IEEE Trans. Wireless Commun.*, vol. 13, no. 9, pp. 4794–4806, Sep. 2014.
[26] D. Korpi, L. Anttila, V. Syrjälä, and M. Valkama, "Widely linear digital self-interference cancellation in direct-conversion full-duplex transceiver," *IEEE J. Sel. Areas Commun.*, vol. 32, no. 9, pp. 1674–1687, Sep. 2014.
[27] R. Li, A. Masmoudi, and T. Le-Ngoc, "Self-interference cancellation with nonlinearity and phase-noise suppression in full-duplex systems," *IEEE Trans. Veh. Technol.*, vol. 67, no. 3, pp. 2118–2129, Mar. 2018.
[28] M. Duarte, "Full-duplex wireless: Design, implementation and characterization," Ph.D. dissertation, Dept. Elect. Eng., Rice Univ., Houston, TX, USA, 2012.
[29] A. A. Boulogeorgos, H. A. B. Salameh, and G. K. Karagiannidis, "Spectrum sensing in full-duplex cognitive radio networks under hardware imperfections," *IEEE Trans. Veh. Technol.*, vol. 66, no. 3, pp. 2072–2084, Mar. 2017.
[30] M. Baghani, A. Mohammadi, M. Majidi, and M. Valkama, "Analysis and rate optimization of OFDM-based cognitive radio networks under power amplifier nonlinearity," *IEEE Trans. Commun.*, vol. 62, no. 10, pp. 3410–3419, Oct. 2014.
[31] B. Lim and Y. Ko, "SIR analysis of OFDM and GFDM waveforms with timing offset, CFO, and phase noise," *IEEE Trans. Wireless Commun.*, vol. 16, no. 10, pp. 6979–6990, Oct. 2017.
[32] S. Han, Y. Sung, and Y. H. Lee, "Filter design for generalized frequency-division multiplexing," *IEEE Trans. Signal Process.*, vol. 65, no. 7, pp. 1644–1659, Apr. 2017.
[33] H. Cheng, Y. Xia, Y. Huang, L. Yang, and D. P. Mandic, "Joint channel estimation and Tx/Rx I/Q imbalance compensation for GFDM systems," *IEEE Trans. Wireless Commun.*, vol. 18, no. 2, pp. 1304–1317, Feb. 2019.
[34] S. Kusaladharma and C. Tellambura, "Aggregate interference analysis for underlay cognitive radio networks," *IEEE Wireless Commun. Lett.*, vol. 1, no. 6, pp. 641–644, Dec. 2012.
[35] A. Mohammadian, M. Baghani, and C. Tellambura, "Optimal power allocation of GFDM secondary links with power amplifier nonlinearity and ACI," *IEEE Wireless Commun. Lett.*, vol. 8, no. 1, pp. 93–96, Feb. 2019.
[36] A. Mohammadian, C. Tellambura, and M. Valkama, "Analysis of self-interference cancellation under phase noise, CFO, and IQ imbalance in GFDM full-duplex transceivers," *IEEE Trans. Veh. Technol.*, vol. 69, no. 1, pp. 700–713, Jan. 2020.
[37] S. Parsaeefard, R. Dawadi, M. Derakhshani, T. Le-Ngoc, and M. Baghani, "Dynamic resource allocation for virtualized wireless networks in massive-MIMO-aided and fronthaul-limited C-RAN," *IEEE Trans. Veh. Technol.*, vol. 66, no. 10, pp. 9512–9520, Oct. 2017.
[38] A. Mohammadian and C. Tellambura, "GFDM-modulated full-duplex cognitive radio networks in the presence of RF impairments," in *Proc. IEEE 30th Annu. Int. Symp. Pers. Indoor Mobile Radio Commun. (PIMRC)*, Istanbul, Turkey, Sep. 2019, pp. 1–6.
[39] W. Chung, D. Hong, R. Wichman, and T. Riihonen "Interference cancellation architecture for full-duplex system with GFDM signaling," in *Proc. 24th Eur. Signal Process. Conf. (EUSIPCO)*, Budapest, Hungary, 2016, pp. 788–792.
[40] A. Mohammadian and C. Tellambura, "Full-duplex GFDM radio transceivers in the presence of phase noise, CFO and IQ imbalance," in *Proc. IEEE Int. Conf. Commun. (ICC)*, Shanghai, China, May 2019, pp. 1–6.
[41] H. Moazzen, A. Mohammadi, and M. Majidi, "Performance analysis of linear precoded MU-MIMO-OFDM systems with nonlinear power amplifiers and correlated channel," *IEEE Trans. Commun.*, vol. 67, no. 10, pp. 6753–6765, Oct. 2019.
[42] S. Teodoro, A. Silva, R. Dinis, F. M. Barradas, P. M. Cabral, and A. Gameiro, "Theoretical analysis of nonlinear amplification effects in massive MIMO systems," *IEEE Access*, vol. 7, pp. 172277–172289, 2019.
[43] M. Baghani, S. Parsaeefard, M. Derakhshani, and W. Saad, "Dynamic non-orthogonal multiple access and orthogonal multiple access in 5G wireless networks," *IEEE Trans. Commun.*, vol. 67, no. 9, pp. 6360–6373, Sep. 2019.
[44] H. Qian, S. Yao, H. Huang, and W. Feng, "A low-complexity digital predistortion algorithm for power amplifier linearization," *IEEE Trans. Broadcast.*, vol. 60, no. 4, pp. 670–678, Dec. 2014.
[45] R. J. Baxley, C. Zhao, and G. T. Zhou, "Constrained clipping for crest factor reduction in OFDM," *IEEE Trans. Broadcast.*, vol. 52, no. 4, pp. 570–575, Dec. 2006.
[46] S. Atapattu, C. Tellambura, and H. Jiang, *Energy Detection for Spectrum Sensing in Cognitive Radio*. New York, NY, USA: Springer, 2014.
[47] S. Atapattu, C. Tellambura, and H. Jiang, "Energy detection of primary signals over η–μ fading channels," in *Proc. Int. Conf. Ind. Inf. Syst. (ICIIS)*, Sri Lanka, Dec. 2009, pp. 118–122.
[48] Z. Sharifian, M. J. Omidi, A. Farhang, and H. Saeedi-Sourck, "Polynomial-based compressing and iterative expanding for PAPR reduction in GFDM," in *Proc. 23rd Iran. Conf. Elect. Eng.*, Tehran, Iran, 2015, pp. 518–523.
[49] K. Liu, W. Deng, and Y. Liu, "An efficient nonlinear companding transform method for PAPR reduction of GFDM signals," in *Proc. IEEE/CIC Int. Conf. Commun. China (ICCC)*, Beijing, China, 2018, pp. 460–464.

AMIRHOSSEIN MOHAMMADIAN (Student Member, IEEE) received the B.Sc. and M.Sc. degrees in electrical engineering from the Amirkabir University of Technology, Tehran, Iran, in 2014 and 2017, respectively. He is currently pursuing the Ph.D. degree in electrical engineering with the University of Alberta, Edmonton, AB, Canada. His current research interests include wireless communication, full-duplex transmission, cognitive radio networks, dirty RF, and MIMO structure.

CHINTHA TELLAMBURA (Fellow, IEEE) received the B.Sc. degree in electronics and telecommunications from the University of Moratuwa, Sri Lanka, the M.Sc. degree in electronics from the Kings College, University of London, and the Ph.D. degree in electrical engineering from the University of Victoria, Canada.

He was with Monash University, Australia, from 1997 to 2002. Since 2002, he has been with the Department of Electrical and Computer Engineering, University of Alberta, where he is currently a Full Professor. He has authored or coauthored over 560 journal and conference papers, with an H-index of 72 (Google scholar). He has supervised or co-supervised 66 M.Sc., Ph.D., and PDF trainees. His current research interests include cognitive radio, heterogeneous cellular networks, fifth-generation wireless networks, and machine learning algorithms. He received the Best Paper Awards from the IEEE International Conference on Communications in 2012 and 2017. He is the winner of the prestigious McCalla Professorship and the Killam Annual Professorship from the University of Alberta. He served as an Editor for the IEEE TRANSACTIONS ON COMMUNICATIONS from 1999 to 2012, and the IEEE TRANSACTIONS ON WIRELESS COMMUNICATIONS from 2001 to 2007. He was an Area Editor of *Wireless Communications Systems and Theory* from 2007 to 2012. He was elected as a Fellow of the Canadian Academy of Engineering in 2017.